

An optimally convergent smooth blended B-spline construction for unstructured quadrilateral and hexahedral meshes

Kim Jie Koh^a, Deepesh Toshniwal^b, Fehmi Cirak^{a,*}

^a*Department of Engineering, University of Cambridge, Cambridge, CB2 1PZ, UK*

^b*Delft Institute of Applied Mathematics, TU Delft, 628 XE Delft, The Netherlands*

Abstract

Easy to construct and optimally convergent generalisations of B-splines to unstructured meshes are essential for the application of isogeometric analysis to domains with non-trivial topologies. Nonetheless, especially for hexahedral meshes, the construction of smooth and optimally convergent isogeometric analysis basis functions is still an open question. We introduce a simple partition of unity construction that yields smooth blended B-splines on unstructured quadrilateral and hexahedral meshes. The new basis functions, referred to as SB-splines, are obtained by, first, defining a linearly independent set of mixed smoothness splines that are C^0 continuous in the unstructured regions of the mesh and have higher smoothness everywhere else. Next, globally smooth linearly independent splines are obtained by smoothly blending the set of mixed smoothness splines with Bernstein basis functions of equal degree. One of the key novelties of our approach is that the required smooth weight functions are obtained from the first set of mixed smoothness splines. The obtained SB-splines are smooth, non-negative, have no breakpoints within the elements and reduce to conventional B-splines away from the extraordinary features in the mesh. Although we consider only quadratic B-splines in this paper, the construction carries over to arbitrary degrees. We demonstrate the excellent performance and optimal convergence of the SB-splines studying Poisson and biharmonic problems in one, two and three dimensions.

Keywords: isogeometric analysis, B-splines, smooth splines, quadrilateral meshes, hexahedral meshes

1. Introduction

The smoothness of spline basis functions is vital in the isogeometric analysis of problems with higher-order partial differential equations. For instance, gradient-theories of elasticity and plasticity [1–5], phase-field modelling of sharp interfaces [6–8] and Kirchhoff-Love type plate and shell models [9–12] and their extensions [13, 14] all lead to higher-order partial differential equations. Since its inception, isogeometric analysis brought about a revival of such theories mainly because of the ease of discretising higher-order partial differential equations using smooth spline basis functions. In particular, smooth basis functions avoid the introduction of (non-physical) extra degrees of freedom and promise a better integration with common computer-aided design representations. However, standard spline basis functions, including B-splines, NURBS and box-splines, are defined only on structured meshes and must be suitably extended for domains with non-trivial topology. For instance, multivariate B-splines are defined only on structured quadrilateral and hexahedral meshes in 2D and 3D, respectively. Most industrial complex geometries cannot be parametrised with a structured mesh so that a limited number of singularities on the surface or inside the volume must be introduced [15–23]. These singularities manifest themselves as extraordinary vertices and edges in the mesh, see Figure 1. For a hexahedral mesh, an interior vertex is extraordinary if it is not incident to 8 hexahedra, and an interior edge is extraordinary if it is not incident to 4 hexahedra. Similarly, an interior vertex is extraordinary for a quadrilateral mesh if it is not incident to 4. The construction of smooth splines which generalise or extend B-splines to unstructured meshes is currently a very active area of research in isogeometric analysis.

*Corresponding author

Email address: f.cirak@eng.cam.ac.uk (Fehmi Cirak)

Table 1: Summary of the terminology and symbols used in this paper. Note that this terminology, in particular the usage of *blending* or *blended* is not uniform across the isogeometric analysis and geometric design literature.

Terminology	Definition
Mixed B-splines, $\mathbf{B}(\mathbf{x})$	B-splines of mixed smoothness.
Blending	Combination of different basis functions using weight functions.
SB-splines, $\mathbf{N}(\mathbf{x})$	Smooth blended splines obtained by the proposed construction.

In computer-aided design numerous constructions have been proposed to deal with extraordinary vertices in a surface mesh, including geometrically G^k and parametrically C^k continuous constructions [24–33], subdivision surfaces [34–40] and manifold constructions [41–47]. There is, however, a very limited number of constructions for volume meshes, including [48–53]; most likely because conventional computer-aided design representations do not require a volume parametrisation. As widely reported, most constructions from computer-aided design do not lead in isogeometric analysis to optimally convergent finite elements, especially when applied to higher-order partial differential equations, see the discussion in [29]. There are, however, constructions for unstructured quadrilateral meshes, including [30, 32, 38, 45, 46], which yield optimal or nearly optimal convergence rates. In contrast, there are no B-spline based optimally convergent smooth constructions for unstructured hexahedral meshes. Currently, optimality is achieved by either reducing continuity to C^0 around extraordinary features [53–55], combining B-splines with meshless approximants [56] or resorting to non-standard spline definitions [57]. The first approach is not suitable for higher-order partial differential equations whereas the latter approaches lead to schemes that are usually computationally very costly.

In this paper, we derive a computationally efficient, easy to construct and optimally convergent extension of B-splines to unstructured quadrilateral and hexahedral meshes. We dub the new basis functions *SB-splines*; see Table 1 for the terminology used throughout this paper. Although we consider only quadratic B-splines, the presented ideas should carry over to arbitrary degrees. To begin with, we determine on the given unstructured mesh a set of B-splines of mixed smoothness following the construction for quadrilateral meshes presented in Toshniwal [58]. The mixed B-splines are C^0 continuous around extraordinary features, i.e. extraordinary vertices (in 2D and 3D) and extraordinary edges (in 3D), but are C^1 smooth everywhere else. Subsequently, we use the partition of unity method of Melenk and Babuška [59] to blend the mixed B-splines $\mathbf{B}(\mathbf{x})$ with Bernstein basis functions $\mathbf{Q}(\mathbf{x})$ of equal degree. To this end, a set of smooth weight, or partition of unity, functions $w^B(\mathbf{x})$ and $w^Q(\mathbf{x})$ are defined to blend both types of basis functions. A key novelty of our approach is that the blending function $w^B(\mathbf{x})$ is assembled from the mixed B-splines on the unstructured mesh, by excluding the C^0 ones, so that $w^Q(\mathbf{x}) := 1 - w^B(\mathbf{x})$. Consequently, the weight functions $w^B(\mathbf{x})$ and $w^Q(\mathbf{x})$ are C^1 smooth and have their breakpoints at the element boundaries. On

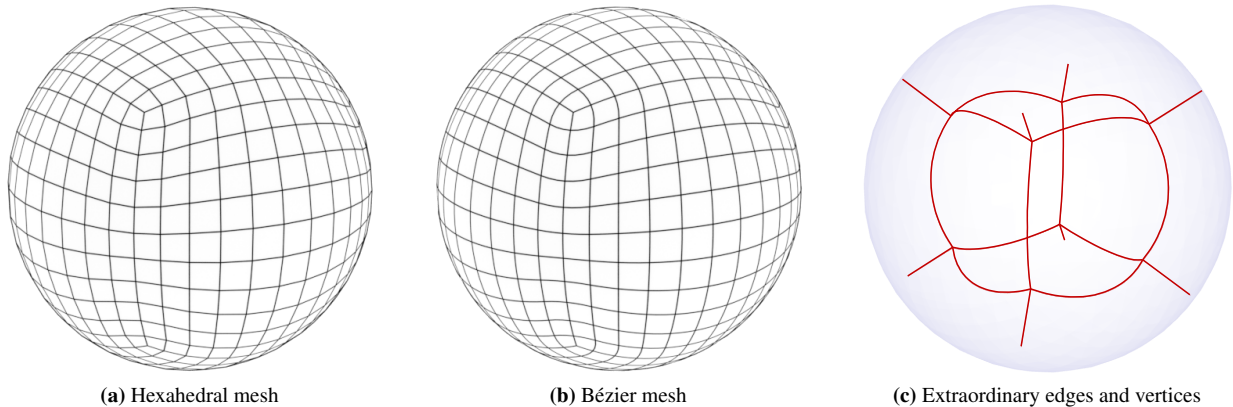


Figure 1: Spherical domain discretised with a hexahedral mesh containing extraordinary edges and vertices. The Bézier mesh represents the physical domain.

quadrilateral meshes with extraordinary vertices the SB-splines are simply given by the weighted basis functions $w^B(\mathbf{x})\mathbf{B}(\mathbf{x})$ and $w^Q(\mathbf{x})\mathbf{Q}(\mathbf{x})$. In hexahedral meshes, the extraordinary edges and vertices usually form a connected network as illustrated in Figure 1c; see also relevant work on hexahedral meshing [15–23]. That is, the weight function $w^Q(\mathbf{x}) = 1 - w^B(\mathbf{x})$ has a support over the entire network and is decomposed as $w^Q(\mathbf{x}) = \sum_i \sum_j w_{i,j}^P(\mathbf{x}) + \sum_j w_j^J(\mathbf{x})$ into locally supported weight functions. In brief, the support of one weight function $w_j^J(\mathbf{x})$ covers a region where more than two extraordinary edges meet, and the supports of the weight functions $w_{i,j}^P(\mathbf{x})$ are restricted to the remaining regions along the connecting extraordinary edge chains.

The proposed approach uses, like the manifold-based constructions [43–47], the partition of unity method to smoothly blend mixed B-splines with C^∞ continuous Bernstein basis functions. Unlike manifold-based constructions, the two types of basis functions are blended in the Euclidean ambient space, i.e. \mathbb{R}^2 in 2D and \mathbb{R}^3 in 3D. Thus, for blending we do not use an atlas consisting of charts and smooth transitions maps. Although it is easy to devise smooth transition maps for 2-manifolds, e.g. using conformal or characteristic maps [36, 43], it is not clear how to construct them in \mathbb{R}^3 . Circumventing the need for such a smooth atlas yields a conceptually and implementation-wise simpler approach and smooth basis functions with appealing properties. The SB-splines are obtained by blending polynomials defined either on the parameter or ambient space and, hence, can be integrated very efficiently using standard Gauss-Legendre quadrature. Furthermore, the weight functions $w^B(\mathbf{x})$ and $w^Q(\mathbf{x})$ have minimal polynomial degree considering that they are assembled from B-splines and their complements to one.

The outline of this paper is as follows. To begin with, we briefly discuss in Section 2 the construction of SB-splines in 1D to introduce the key ideas and terminology used throughout the paper. Subsequently, we consider in Section 3 the construction of SB-splines on unstructured quadrilateral meshes with extraordinary vertices. We first review the mixed B-splines in Section 3.1 and then discuss the construction of SB-splines, in particular the weight functions, in Section 3.2. As explained in Section 3.2.1, it is straightforward to derive closed form expressions of the new basis functions for use in existing isogeometric analysis implementations. In Section 4, we consider the construction of SB-splines on unstructured hexahedral meshes with extraordinary edges and vertices. After discussing the extension of mixed B-splines to hexahedral meshes in Section 4.1, we first introduce the notion of an *extraordinary prism* and *extraordinary joint* and discuss how to construct the respective weight and smooth basis functions in Section 4.2. Finally, we introduce in Section 5 several Poisson and biharmonic examples to confirm the convergence of the SB-splines. We study in particular the influence of the number of quadrature points and the valence of the extraordinary vertices on finite element convergence in 2D. The paper is supplemented by four appendices that provide a proof of linear independence and discuss aspects of finite element discretisation, mesh refinement and an illustration of the treatment of arbitrary hexahedral meshes.

2. One-dimensional SB-splines

The proposed construction is best illustrated in the one-dimensional setting. Given is a domain $\Omega \subset \mathbb{R}$ with the parametrisation

$$x(\xi) = \sum_{i=1}^{n_B} B_i(\xi) x_i \quad \text{with } \xi \in \hat{\Omega} := [0, 1], \quad (1)$$

where $B_i(\xi)$ are the univariate B-splines of degree $p_B \geq 2$ and x_i are the coordinates of the control points. As mentioned earlier, in higher dimensions we will focus solely on the case $p_B = 2$. The B-splines $B_i(\xi)$ are defined on the parametric domain $\hat{\Omega}$ with the parametric coordinate ξ . For the sake of illustration, they are chosen to be C^0 continuous at the break point ξ_{ep} and C^{p_B-1} continuous at every other break point. Hence, the point with the coordinate $x_{\text{ep}} := x(\xi_{\text{ep}})$ is an extraordinary point.

Assuming that the parametrisation $x(\xi)$ is, as usual, bijective, the push-forward of the basis functions on the physical domain of interest Ω are given by

$$B_i(x) = B_i(\xi) \circ x(\xi)^{-1} \quad (2)$$

For later reference, the basis functions on the physical domain Ω are collected in the array

$$\mathbf{B}(x) = \begin{pmatrix} B_1(x) & \dots & B_{n_B}(x) \end{pmatrix}^\top. \quad (3)$$

In the neighbourhood of the extraordinary point x_{ep} , we aim to blend the B-splines $\mathbf{B}(x)$ with a second polynomial basis defined only over the the blending domain $\Omega^Q \subset \Omega$. The second basis is, without loss of generality, throughout this paper a Bernstein basis with the basis functions

$$\mathbf{Q}(x) = \begin{pmatrix} Q_1(x) & \dots & Q_{n_Q}(x) \end{pmatrix}^T, \quad (4)$$

where $n_Q = p_Q + 1$ and p_Q is the polynomial degree of the Bernstein basis.

For blending together the two sets of basis functions, we choose a weight function $w^Q(x)$ with $\text{supp } w^Q(x) = \Omega^Q$ and its complement to one $w^B(x)$, i.e.,

$$w^Q(x) + w^B(x) \equiv 1 \quad \forall x \in \Omega. \quad (5)$$

Such weight functions can be chosen in many different ways. In the proposed construction, we assemble the weight function $w^B(x)$ from the B-splines $B_i(x)$. In particular, with the index set $\mathcal{I} = \{i \mid B_i(x) \text{ is at most } C^0 \text{ at } x_{\text{ep}}\}$ and its complement \mathcal{I}^C the weight function is given by

$$w^B(x) = \sum_{i \in \mathcal{I}^C} B_i(x). \quad (6)$$

The so-assembled weight functions have the following properties.

Proposition 1. *The weight functions $w^B(x)$ and $w^Q(x)$ are at least C^1 smooth, piecewise polynomials in the parameter space, have local support and form a partition of unity.*

Finally, using the above set of weight and basis functions, we define the smooth blended B-splines, or SB-splines, as

$$\mathbf{N}(x) = \begin{pmatrix} w^B(x) \mathbf{B}(x)^T & w^Q(x) \mathbf{Q}(x)^T \end{pmatrix}^T = \begin{pmatrix} N_1(x) & \dots & N_{n_N}(x) \end{pmatrix}^T, \quad (7)$$

where $n_N = n_B + n_Q$. Evidently, the smoothness, the support size and the polynomial degree of the SB-splines depend on the properties of $\mathbf{B}(x)$, $\mathbf{Q}(x)$, $w^B(x)$ and $w^Q(x)$. Critical for the smoothness properties of the SB-splines is the choice of the weight function $w^B(x)$.

Proposition 2. *The SB-splines $\mathbf{N}(x)$ are at least C^1 smooth, linearly independent, non-negative, have local support and form a partition of unity.*

The properties of smoothness, non-negativity, local support and partition of unity follow directly from the blending construction since both $\mathbf{B}(x)$ and $\mathbf{Q}(x)$ possess these properties. For the proof of linear independence, see [Appendix A](#).

As a concrete example, Figure 2 illustrates the blending of mixed smoothness quadratic B-splines $\mathbf{B}(x)$ with quadratic Bernstein basis functions $\mathbf{Q}(x)$. The physical domain Ω has at its centre an extraordinary point with C^0 continuity, introduced using a non-uniform open knot vector for $\mathbf{B}(x)$. Except at the extraordinary point the quadratic B-spline basis $\mathbf{B}(x)$ is C^1 smooth. The weight function $w^B(x)$ is assembled from B-splines $B_i(x)$ by excluding the ones which are at most C^0 smooth at the extraordinary point. Hence, the weight function $w^B(x)$ and, in turn, its complement $w^Q(x) = 1 - w^B(x)$ are intrinsically C^1 smooth. The blending domain Ω^Q is equal to the support of the weight function $w^Q(x)$. After determining the weight functions it is straightforward to compute the basis functions $N_i(x)$ depicted in Figures 2c and 2d, which are all C^1 smooth. We emphasise that a key aspect of our construction is that the weight function $w^B(x)$ is assembled from the smooth B-splines $\mathbf{B}(x)$. As apparent in Figure 2a, outside the blending region Ω^Q the weight function $w^B(x)$ is equal to one so that the SB-splines are equal to the standard B-splines.

Evidently, the proposed construction can be applied to B-splines of any degree. Figure 3 illustrates the blending of mixed smoothness cubic B-splines and cubic Bernstein basis functions. The SB-splines depicted in Figures 3c and 3d are also C^1 continuous. In the next sections, we restrict our attention to $p_B = p_Q = 2$.

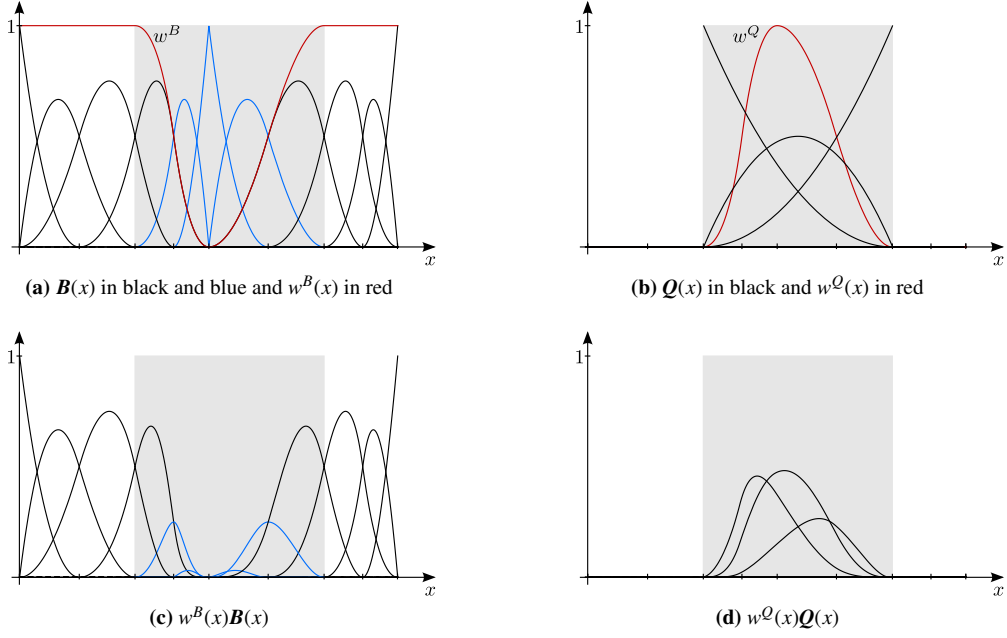


Figure 2: Blending of the mixed smoothness quadratic B-splines $\mathbf{B}(x)$ in (a) with the quadratic Bernstein basis functions $\mathbf{Q}(x)$ in (b). The non-uniform open knot vector for the B-splines $\mathbf{B}(x)$ has repeated knot values at the boundaries and at the extraordinary point at the centre of the physical domain Ω . In (a) the B-splines in blue are C^0 continuous at the extraordinary point. The blending domain Ω^Q is shaded in grey. The weight function $w^B(x)$ in (a) is the sum of the B-spline basis functions which are C^1 smooth at the extraordinary point. Its complement to one is the weight function $w^Q(x)$ in (b).

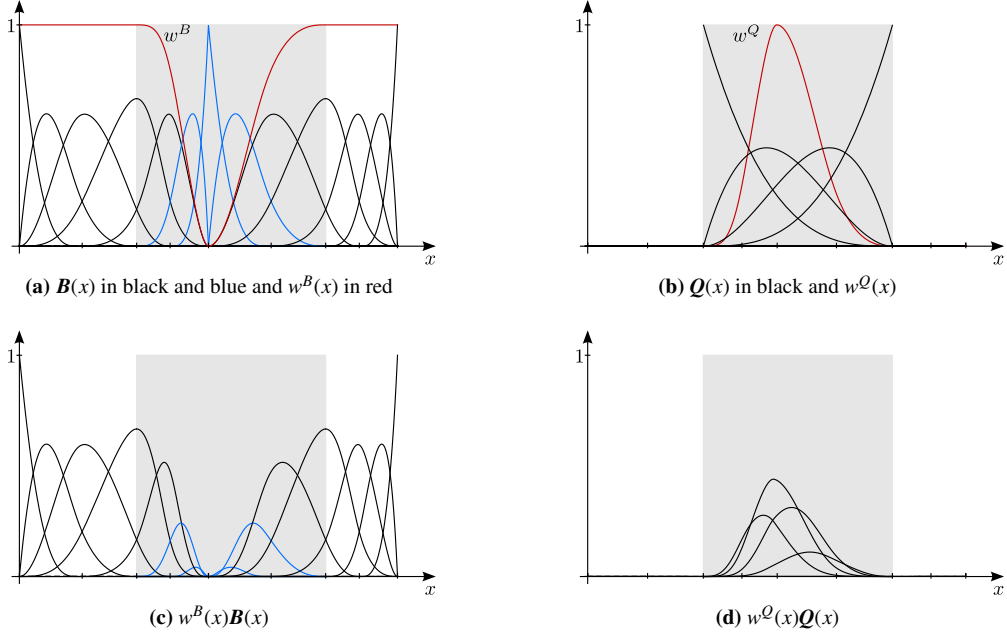


Figure 3: Blending of the mixed smoothness cubic B-splines $\mathbf{B}(x)$ in (a) with the cubic Bernstein basis functions $\mathbf{Q}(x)$ in (b). The non-uniform open knot vector for the B-splines $\mathbf{B}(x)$ has repeated knot values at the boundaries and at the extraordinary point at the centre of the physical domain Ω . In (a) the B-splines in blue are C^0 continuous at the extraordinary point. The blending domain Ω^Q is shaded in grey. The weight function $w^B(x)$ in (a) is the sum of the B-spline basis functions which are at least C^1 smooth at the domain centre. Its complement to one is the weight function $w^Q(x)$ in (b).

3. Two-dimensional quadratic SB-splines

We are given an unstructured quadrilateral mesh describing a domain $\Omega \subset \mathbb{R}^2$. The mesh consists of elements, i.e. quadrilateral faces, and their edges and vertices. We assume that all the vertices on the boundary of the mesh are regular, i.e. are adjacent to two elements, and all the extraordinary vertices within the mesh, i.e. vertices with other than four adjacent elements, are sufficiently separated as to be specified. If not the case, this can be achieved by successive quadrisection refinement of all elements. The new vertices introduced during refinement are all regular so that the extraordinary vertices become more and more separated. In the following, without loss of generality, we focus on bi-quadratic B-splines and assume that the mesh has a single extraordinary vertex of valence $v \neq 4$. In the (locally) structured regions of the mesh standard smooth tensor-product bi-quadratic B-splines can be defined. It is impossible to define such B-splines in the 1-neighbourhood of an extraordinary vertex due to the lack of a tensor-product mesh structure. A 1-neighbourhood of a vertex is formed by the union of the elements that contain the vertex. The n -neighbourhood is defined recursively as the union of all 1-neighbourhoods of all the vertices in the $(n-1)$ -neighbourhood. With this definition at hand, we require that the 3-neighbourhoods of the extraordinary vertices in the considered mesh are disjoint.

3.1. Review of mixed B-splines

Although it is not possible to define a standard tensor-product B-spline basis on an unstructured mesh, it is possible to construct a B-spline basis of mixed smoothness; see Toshniwal [58]. The mixed B-splines are C^1 continuous away from the 1-neighbourhood of extraordinary vertices and are C^0 continuous along mesh edges adjacent to extraordinary vertices. That is, away from the 1-neighbourhood of extraordinary vertices the mixed B-splines are identical to tensor-product B-splines. On structured meshes there is a one-to-one correspondence between the bi-quadratic B-splines and elements (away from the boundaries). This is also the case for mixed B-splines. Hence, we can assign a control vertex to each element. The support of a mixed B-spline consists of all elements sharing a vertex with the respective element.

We represent the non-zero mixed B-splines within an element with bi-quadratic Bézier basis functions. The control vertices of the mixed B-splines are denoted with $\mathbf{x}_i \in \mathbb{R}^2$ and the ones of the Bézier basis functions with $\mathbf{c}_j \in \mathbb{R}^2$. The numbering of both sets of control vertices is given in Figure 4a. We define the mixed B-splines by first establishing the map from the control vertices \mathbf{x}_i to \mathbf{c}_j . To this end, the Bézier control vertices are expressed as linear combinations of the mixed B-spline control vertices. The corresponding weights can be graphically visualised with the masks shown in Figures 4b and 4c. The edge Bézier control vertices $\mathbf{c}_2, \mathbf{c}_4, \mathbf{c}_6$ and \mathbf{c}_8 are determined using the mask in Figure 4b and the corner Bézier control vertices $\mathbf{c}_1, \mathbf{c}_2, \mathbf{c}_3$ and \mathbf{c}_4 using the mask in Figure 4c. The centre Bézier control vertex \mathbf{c}_5 has the same value as the mixed B-spline control vertex \mathbf{x}_5 . Finally, the mapping of the mixed B-spline control vertices \mathbf{x}_i to the Bézier control vertices \mathbf{c}_j is given by

$$\begin{pmatrix} \mathbf{c}_1 \\ \mathbf{c}_2 \\ \mathbf{c}_3 \\ \mathbf{c}_4 \\ \mathbf{c}_5 \\ \mathbf{c}_6 \\ \mathbf{c}_7 \\ \mathbf{c}_8 \\ \mathbf{c}_9 \end{pmatrix} = \begin{pmatrix} \frac{1}{4} & \frac{1}{4} & 0 & \frac{1}{4} & \frac{1}{4} & 0 & 0 & 0 & \cdots & 0 \\ 0 & \frac{1}{2} & 0 & 0 & \frac{1}{2} & 0 & 0 & 0 & \cdots & 0 \\ 0 & \frac{1}{4} & \frac{1}{4} & 0 & \frac{1}{4} & \frac{1}{4} & 0 & 0 & \cdots & 0 \\ 0 & 0 & 0 & \frac{1}{2} & \frac{1}{2} & 0 & 0 & 0 & \cdots & 0 \\ 0 & 0 & 0 & 0 & 1 & 0 & 0 & 0 & \cdots & 0 \\ 0 & 0 & 0 & 0 & \frac{1}{2} & \frac{1}{2} & 0 & 0 & \cdots & 0 \\ 0 & 0 & 0 & \frac{1}{4} & \frac{1}{4} & 0 & \frac{1}{4} & \frac{1}{4} & \cdots & 0 \\ 0 & 0 & 0 & 0 & \frac{1}{2} & 0 & 0 & \frac{1}{2} & \cdots & 0 \\ 0 & 0 & 0 & 0 & \frac{1}{v} & \frac{1}{v} & 0 & \frac{1}{v} & \cdots & \frac{1}{v} \end{pmatrix} \begin{pmatrix} \mathbf{x}_1 \\ \mathbf{x}_2 \\ \mathbf{x}_3 \\ \mathbf{x}_4 \\ \mathbf{x}_5 \\ \mathbf{x}_6 \\ \mathbf{x}_7 \\ \mathbf{x}_8 \\ \mathbf{x}_{9+v-4} \end{pmatrix} \Rightarrow \mathbf{c}_j = \sum_i M_{ji} \mathbf{x}_i. \quad (8)$$

Combining the Bézier basis functions $Q_j(\boldsymbol{\eta})$ of an element with the map (8) from the control vertices \mathbf{x}_i to \mathbf{c}_j , we can define both a (local) parametrisation of the physical domain Ω and the mixed B-splines $B_i(\mathbf{x})$. Note that the Bézier basis functions $Q_j(\boldsymbol{\eta})$ are local to each element. Specifically, with the mixed B-spline control vertices \mathbf{x}_i given in Figure 4a and the map (8) the geometry parametrisation within the element corresponding to the control vertex \mathbf{x}_5 is given by

$$\mathbf{x}(\boldsymbol{\eta}) = \sum_{j=1}^9 Q_j(\boldsymbol{\eta}) \mathbf{c}_j = \sum_{j=1}^9 \sum_{i=1}^{9+v-4} Q_j(\boldsymbol{\eta}) M_{ji} \mathbf{x}_i \quad \text{with } \boldsymbol{\eta} = (\eta_1, \eta_2) \in \square := [0, 1] \times [0, 1]. \quad (9)$$

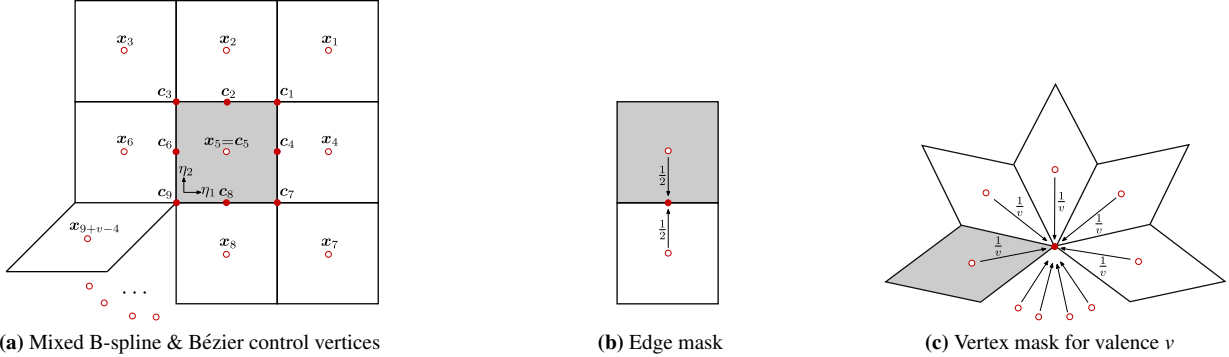


Figure 4: Averaging masks for computing the bi-quadratic Bézier control vertices c_j . The empty circles denote the mixed B-spline control vertices x_i and the solid circles the Bézier control vertices c_j . The corner mask (c) for extraordinary vertices is a straightforward generalisation of the corner mask for ordinary vertex with $v = 4$. The masks (b) and (c) describe a bi-quadratic B-spline when an element's all vertices are regular.

This description also defines the mixed B-spline $B_5(\mathbf{x})$ associated to control vertex x_5 . According to (9), its preimage in the parametric domain is given by

$$B_5(\boldsymbol{\eta}) = \sum_{j=1}^9 Q_j(\boldsymbol{\eta}) M_{j5} \quad (10)$$

such that

$$B_5(\mathbf{x}) = B_5(\boldsymbol{\eta}) \circ \mathbf{x}(\boldsymbol{\eta})^{-1}. \quad (11)$$

The B-splines $B_i(\mathbf{x})$ associated to the other control vertices in the mesh are obtained in the same way. See [58] for other properties of the mixed B-splines.

As an example, the parametrised domain, i.e. Bézier mesh corresponding to the unstructured mesh in Figure 5a with an extraordinary vertex with $v = 5$ is visualised in Figure 5b. The parametrisation is C^1 smooth in most parts of the domain as is suggested by the plotted parameter lines with either $\eta_1 = \text{const.}$ or $\eta_2 = \text{const.}$ It is C^0 continuous across the edges that contain the extraordinary vertex. For a control vertex in the 1-neighbourhood of the extraordinary vertex we obtain the basis function shown in Figure 5c. This basis function is only C^0 continuous across the edges that contain the extraordinary vertex, as can be inferred from the plotted parameter lines.

3.2. Construction of SB-splines

The construction of the blended C^1 smooth basis functions is analogous to 1D. First, we choose a weight function $w^B(\mathbf{x})$ and its complement to one $w^Q(\mathbf{x}) = 1 - w^B(\mathbf{x})$. The weight function $w^B(\mathbf{x})$ is assembled from the smooth mixed B-splines defined on the unstructured mesh. Importantly, the blending of the basis functions takes place in the physical domain Ω rather than the parametric domain of the basis functions. It is impossible to map every multi-dimensional physical domain with arbitrary topology onto a single parametric domain. This can be achieved only by introducing an atlas consisting of several charts with respective parametric domains and transition functions [45–47]. The definition of such smooth transition function on unstructured meshes is usually very challenging. Instead, constructing the weight functions on the physical domain sidesteps the need for an atlas and smooth transition functions.

As discussed in the preceding section smooth mixed B-splines $B_i(\boldsymbol{\eta})$ are defined only away from the 1-neighbourhood of an extraordinary vertex. Furthermore, the mixed B-splines $B_i(\mathbf{x})$ on the physical domain are obtained by mapping $B_i(\boldsymbol{\eta})$ from the reference element via the mapping $\mathbf{x}(\boldsymbol{\eta})^{-1}$, see (11). According to the chain rule of differentiation the smoothness of $B_i(\mathbf{x})$ relies both on the smoothness of $B_i(\boldsymbol{\eta})$ and $\mathbf{x}(\boldsymbol{\eta})^{-1}$. This implies that beyond the 1-neighbourhood of an extraordinary vertex most of the control vertices in its 2-neighbourhood belong to non-smooth mixed B-splines $B_i(\mathbf{x})$ as well, see Figure 6a.

We assemble the weight function $w^B(\mathbf{x})$ from the mixed B-splines $B_i(\mathbf{x})$ by excluding the ones belonging to the control vertices in the 2-neighbourhood of the extraordinary vertex, i.e. by excluding the mixed B-splines associated

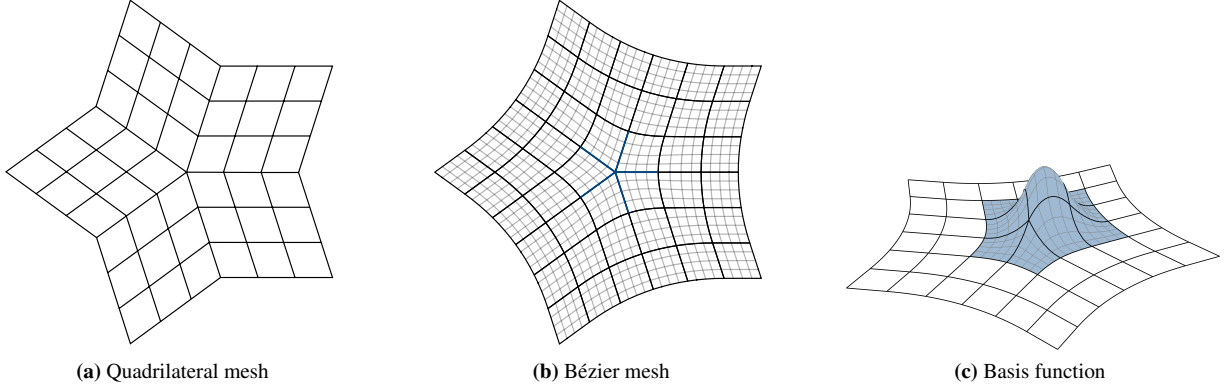


Figure 5: Unstructured quadrilateral mesh with only one extraordinary vertex with valence $v = 5$, its parametrisation and the graph of one of the corresponding basis functions. The thin lines in (b) and (c) indicate the parameter lines with either $\eta_1 = \text{const.}$ or $\eta_2 = \text{const.}$ In the 1-neighbourhood of the extraordinary vertex across the element edges, i.e. the blue edges in (b), the parametrisation is only C^0 continuous and everywhere else it is C^1 smooth.

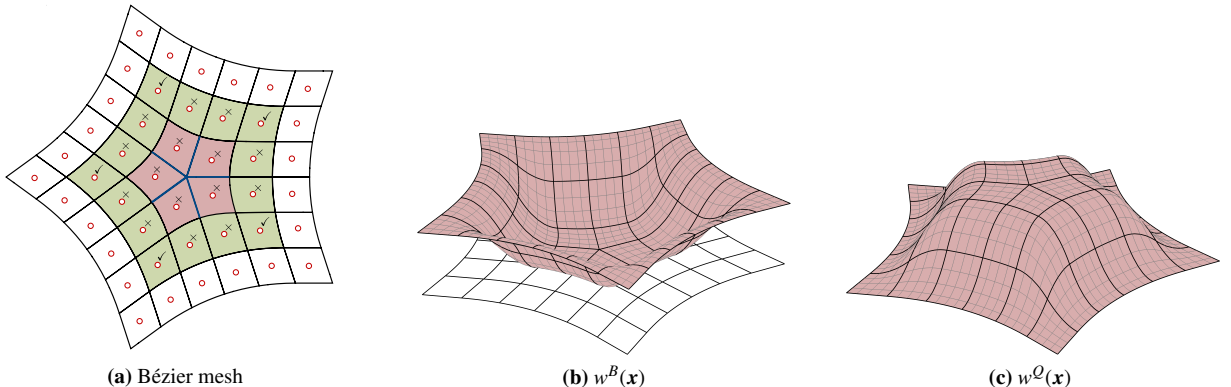


Figure 6: Smoothness of the mixed B-splines $B_i(\mathbf{x})$ and weight functions $w^B(\mathbf{x})$ and $w^Q(\mathbf{x})$. In (a) the mixed B-splines $B_i(\mathbf{x})$ are represented by the respective control vertices (empty circles). In addition, $B_i(\mathbf{x})$ that are C^1 and C^0 continuous across element edges in the 1-neighbourhood of the extraordinary vertex (blue edges) are labelled with ticks and crosses, respectively. In (b) the weight function $w^B(\mathbf{x})$ is assembled by excluding the mixed B-splines $B_i(\mathbf{x})$ belonging to the control vertices in the 2-neighbourhood of the extraordinary vertex. Its complement to one $w^Q(\mathbf{x}) = 1 - w^B(\mathbf{x})$ is shown in (c).

to all control vertices marked with a cross or a tick in Figure 6a. Although only the non-smooth mixed B-splines must be excluded, for ease of implementation we exclude some of the smooth mixed B-splines as well. The so-obtained smooth weight function $w^B(\mathbf{x})$ and its complement to one $w^Q(\mathbf{x}) = 1 - w^B(\mathbf{x})$ are depicted in Figures 6b and 6c, respectively. Evidently, both weight functions are C^1 smooth, bi-quadratic on the reference element domain \square and $\text{supp } w^Q(\mathbf{x})$ is comprised of the 3-neighbourhood of the extraordinary vertex.

Next, we choose a bi-quadratic Bernstein basis $\{Q_j(\mathbf{x})\}_{j=1}^9$ as the second basis for blending. These are defined on a different domain than the ones in (9); indeed, considering that the blending takes place in the physical domain Ω this basis is defined in the physical domain with $\mathbf{x} \in \Omega$. To guarantee the positivity of the SB-splines, the domain of the Bernstein basis $\{Q_j(\mathbf{x})\}_{j=1}^9$ must enclose the blending domain Ω^Q , but can be chosen freely otherwise. As in 1D, the SB-splines are then defined by

$$N(\mathbf{x}) = \begin{pmatrix} w^B(\mathbf{x}) \mathbf{B}(\mathbf{x})^\top & w^Q(\mathbf{x}) \mathbf{Q}(\mathbf{x})^\top \end{pmatrix}^\top \quad (12)$$

with

$$\mathbf{B}(\mathbf{x}) = \begin{pmatrix} B_1(\mathbf{x}) & \dots & B_{n_B}(\mathbf{x}) \end{pmatrix}^\top, \quad \mathbf{Q}(\mathbf{x}) = \begin{pmatrix} Q_1(\mathbf{x}) & \dots & Q_9(\mathbf{x}) \end{pmatrix}^\top. \quad (13)$$

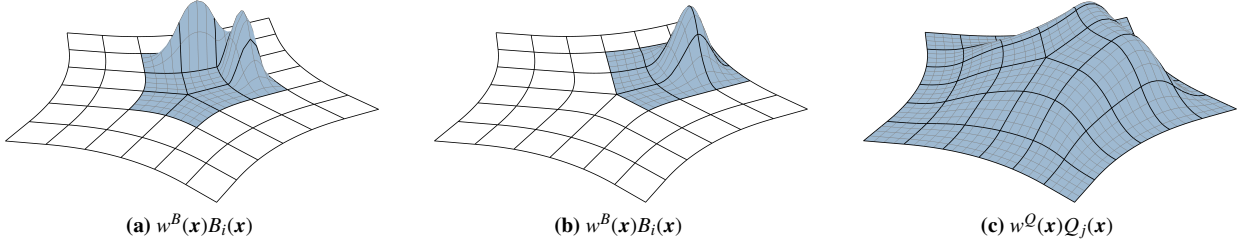


Figure 7: Three of the obtained SB-splines $N_i(\mathbf{x})$. The SB-splines in (a) and (b) correspond to the non-smooth mixed B-splines $B_i(\mathbf{x})$ belonging to the control vertices in the 1-neighbourhood and 2-neighbourhood, respectively. The SB-spline in (c) corresponds to one of the Bézier basis functions $Q_j(\mathbf{x})$.

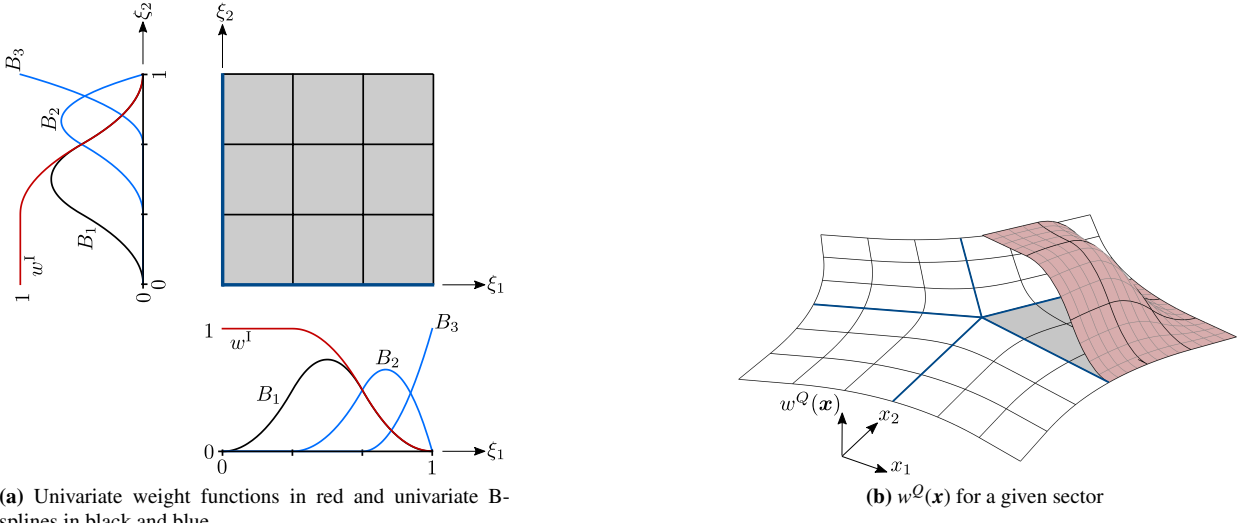


Figure 8: Construction of the weight function $w^Q(\mathbf{x})$ on one of the v sectors in the 3-neighbourhood of an extraordinary vertex. The weight function $w^Q(\xi)$ on the parametric domain $\hat{\Omega}$ is defined as the product of the univariate weight functions $w^I(\xi_1)$ and $w^I(\xi_2)$ in (a). Formally, $w^Q(\mathbf{x})$ on each element on the domain Ω in (b) is given by $w^Q(\mathbf{x}) = w^Q(\xi) \circ \eta(\xi)^{-1} \circ \mathbf{x}(\eta)^{-1}$.

The obtained basis functions $\mathbf{N}(\mathbf{x})$ are C^1 smooth. In Figures 7a and 7b two of the basis functions $w^B(\mathbf{x})B_i(\mathbf{x})$ and in Figure 7c one of the basis functions $w^Q(\mathbf{x})Q_j(\mathbf{x})$ are plotted.

3.2.1. Sector-wise construction

In usual finite element implementations integrals are evaluated in a reference element domain $\square := [0, 1] \times [0, 1]$. To facilitate the element-based implementation of the proposed blended approach, we consider a sector-wise construction of the weight functions $w^B(\mathbf{x})$ and $w^Q(\mathbf{x})$. The process is outlined in Figure 8. The 3-neighbourhood of the extraordinary vertex is partitioned into v sectors. Each sector consisting of 3×3 elements is parametrised with $\xi = (\xi_1, \xi_2) \in \hat{\Omega} := [0, 1] \times [0, 1]$, see Figure 8a. The elements on the parametric domain $\hat{\Omega}$ are mapped using a mapping $\eta(\xi)$ composed of a translation and a scaling to the reference element \square for integration.

With the extraordinary vertex located at the origin $\xi = (0, 0)$ of $\hat{\Omega}$, the implementation of the weight functions is identical on all the v sectors. Therefore, it is sufficient to detail the implementation only one of the sectors. As illustrated in Figure 8b, the weight function $w^Q(\mathbf{x})$ is constructed by first defining $w^Q(\xi)$ on the parametric domain $\hat{\Omega}$. We define $w^Q(\xi)$ as the tensor product of univariate weight functions $w^I(\xi_1)$ and $w^I(\xi_2)$,

$$w^Q(\xi) = w^I(\xi_1) \otimes w^I(\xi_2). \quad (14)$$

First, we assemble along the ξ_1 and ξ_2 axes the univariate weight functions for $w^B(\xi_1)$ and $w^B(\xi_2)$ by excluding the univariate B-splines which are not C^1 smooth at the origin $\xi = (0, 0)$, see Figure 8a. Then, their complements to one

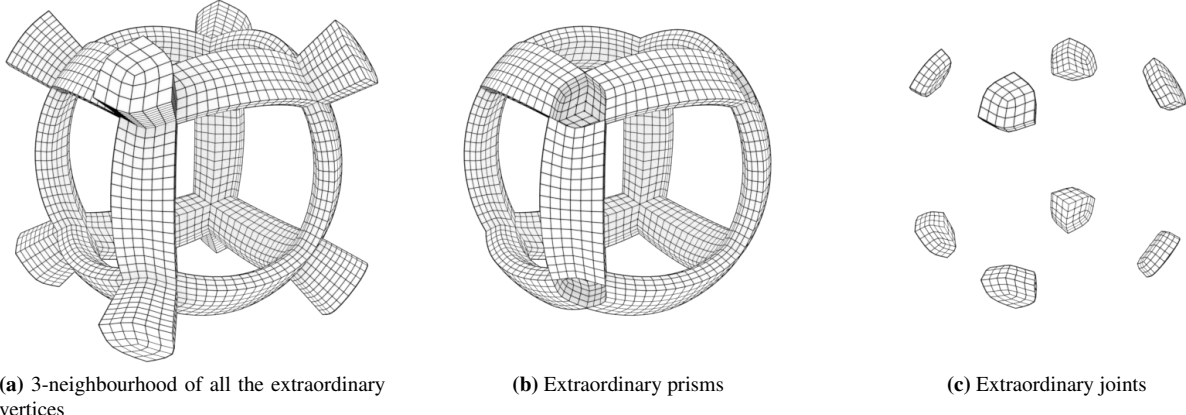


Figure 9: Extraordinary features in the unstructured hexahedral sphere mesh in Figure 1. The 3-neighbourhood of the extraordinary vertices (a) are decomposed into twenty extraordinary prisms (b) and eight extraordinary joints (c). For illustration purposes, only twelve of the twenty extraordinary prisms are depicted in (b). The extraordinary vertices corresponding to the joints have $v = 4$ and the extraordinary edges corresponding to the prisms have $e = 3$.

yield

$$w^I(\xi_i) = 1 - B_2(\xi_i) - B_3(\xi_i), \quad i = 1, 2. \quad (15)$$

For evaluating the finite element integrals the weight function values at the quadrature points in the reference element \square are required, which are obtained from

$$w^Q(\eta) = w^Q(\xi) \circ \eta(\xi)^{-1}. \quad (16)$$

Here, the mapping $\eta(\xi)$ is, as mentioned above, composed of a translation and scaling and can be easily inverted.

4. Three-dimensional quadratic SB-splines

The proposed construction of SB-splines can also be extended to unstructured hexahedral meshes describing a domain $\Omega \subset \mathbb{R}^3$. A mesh consists of elements, i.e. hexahedral cells, their quadrilateral faces, edges and vertices. In 3D there are in addition to extraordinary vertices also extraordinary edges, see Figure 1c. Extraordinary edges are connected to two extraordinary vertices and regular edges to two regular vertices. In this paper, we assume that there are no edges with one ordinary and one extraordinary vertex and that all edges on the boundary of the domain are regular, i.e. are adjacent to two elements. Furthermore, the valence of an edge e is defined as the number of elements that share the same two vertices like the edge.

Well-designed hexahedral finite element meshes consist of a small number of chains of extraordinary edges. There are usually only a few extraordinary vertices with more than two attached extraordinary edges [17, 20]. As in 2D, only the 3-neighbourhood of the extraordinary vertices and extraordinary edges is relevant for the proposed construction. In 3D, the union of the 3-neighbourhoods of all the extraordinary vertices in the mesh form a 6-element wide chain of elements as depicted in Figure 9a. We split the chain into several disjoint sets and refer to them as extraordinary prisms or extraordinary joints as illustrated in Figures 9b and 9c. Joints consist of the 3-neighbourhood of extraordinary vertices where more than two extraordinary edges meet. The remaining elements in the chain form the prisms. Each prism is connected to either a joint or the domain boundary.

In practice, the possible number of extraordinary edges meeting at an extraordinary vertex is limited. For the sake of clarity and conciseness, without loss of generality, we consider in this section only a joint with four attached prisms, i.e. $v = 4$, each of which have valence $e = 3$. The arbitrary v and e case can be similarly elaborated upon as is briefly discussed in [Appendix D](#).

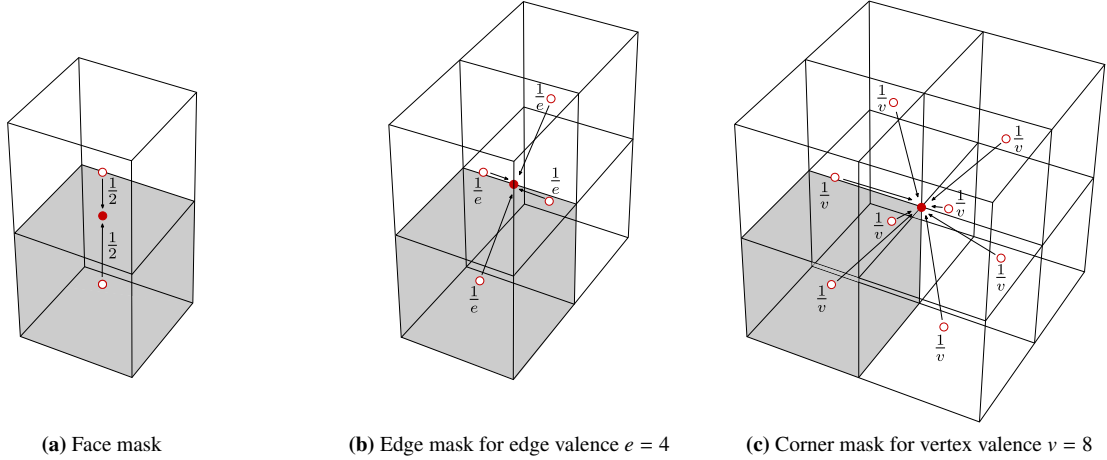


Figure 10: Averaging masks for computing the tri-quadratic Bézier control vertices. The empty circles denote the mixed B-spline control vertices x_i and the solid circles the Bézier control vertices c_j . The averaging masks for the edge Bézier control vertex in (b) and corner Bézier control vertex in (c) depend on the valence of the edge e and the valence of the vertex v , respectively.

4.1. Review of mixed B-splines

We now outline the extension of the mixed B-spline construction in Section 3.1 to an unstructured hexahedral mesh. The resulting tri-quadratic mixed B-splines are C^1 continuous away from the 1-neighbourhood of extraordinary edges and are only C^0 continuous along mesh faces adjacent to extraordinary vertices. Again, there is a one-to-one correspondence between the tri-quadratic mixed B-splines and the elements in the mesh (away from the boundaries) so that we assign a control vertex to each element. The support of the respective mixed B-spline consists of all elements sharing a vertex with the element.

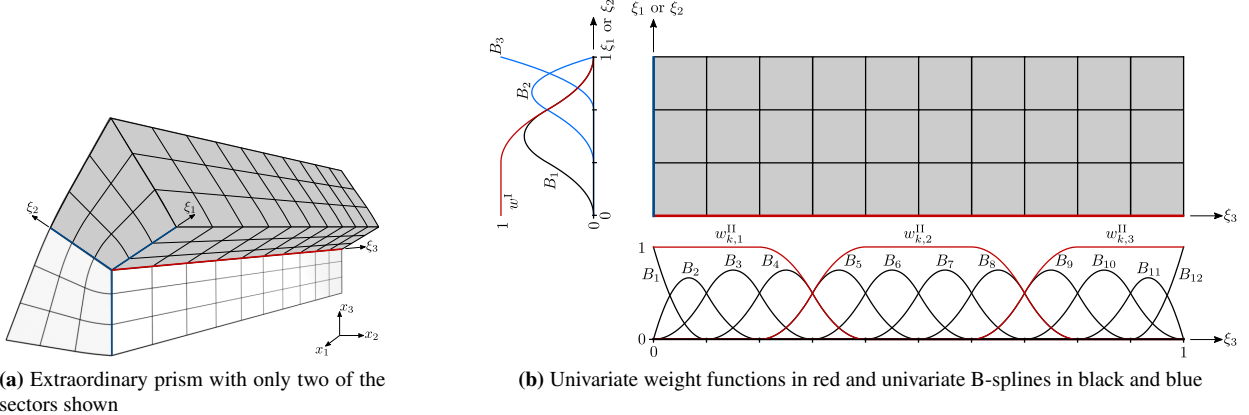
As before, we first represent the non-zero mixed B-splines within an element with tri-quadratic Bézier basis functions. Subsequently, the corresponding Bézier control vertices are expressed as linear combinations of the mixed B-spline control vertices using the masks depicted in Figure 10, the labelling of the vertices has been omitted for simplicity. The face Bézier control vertices are determined using the mask in Figure 10a, the edge Bézier control vertices using the mask in Figure 10b and the corner Bézier control vertices using the mask in 10c. The masks for edge and corner Bézier control vertices depend on the valence of the edge e and the valence of the vertex v , respectively. The centre Bézier control vertex has the same value as the element's respective mixed B-spline control vertex.

As in the two-dimensional case, combining the obtained Bézier basis control vertices with Bézier basis function we can define a (local) parametrisation of the physical domain Ω as well as mixed B-splines. Recall that the parameterisation for the quadrilateral mesh in Section 3.1 was C^0 continuous across all edges adjacent to the extraordinary vertex. For hexahedral meshes the parametrisation is C^0 continuous across all faces adjacent to the extraordinary edge.

4.2. Construction of SB-splines

The construction of the blended C^1 smooth basis functions on unstructured hexahedral meshes follows the 1D and 2D constructions with only slight modification. The key idea is again to consider all the smooth mixed B-splines $B_i(\mathbf{x})$ to define the weight function $w^B(\mathbf{x})$ and its complement to one $w^Q(\mathbf{x}) = 1 - w^B(\mathbf{x})$. A naive implementation of this idea leads on hexahedral meshes to a single weight function $w^Q(\mathbf{x})$ with a support covering all the connected extraordinary prisms and joints in the mesh. Clearly, such a construction will lead to an overly dense stiffness matrix and adversely affect the approximation properties of the SB-splines. Therefore, as will be detailed in the following, the weight function $w^Q(\mathbf{x})$ is partitioned into two sets of locally supported weight functions $w_{k,\ell}^P(\mathbf{x})$ and $w_\ell^J(\mathbf{x})$ such that

$$w^Q(\mathbf{x}) = \sum_{k=1}^{n_P} \sum_{\ell=1}^{n_k} w_{k,\ell}^P(\mathbf{x}) + \sum_{\ell=1}^{n_J} w_\ell^J(\mathbf{x}), \quad (17)$$



(a) Extraordinary prism with only two of the sectors shown

(b) Univariate weight functions in red and univariate B-splines in black and blue

Figure 11: Construction of the weight function for an extraordinary prism. The two ends of the prism are either joined to an extraordinary joint or the boundary of the domain Ω . In (a) only two of the e sectors are shown for visualisation purposes. Each sector consists of $3 \times 3 \times n_{ee}$ elements and has a corresponding (cuboidal) parametric domain $\hat{\Omega}$ as illustrated in (b). The weight functions $w_{k,\ell}^P(\xi)$ for one of the e sectors is defined as the tensor product of the bivariate weight function $w^I(\xi_1) \otimes w^{\text{II}}(\xi_2)$ and the three univariate weight functions $w_{k,1}^{\text{II}}(\xi_3)$, $w_{k,2}^{\text{II}}(\xi_3)$ and $w_{k,3}^{\text{II}}(\xi_3)$.

where n_p is the number of extraordinary prisms, n_k is the number of weight functions defined along the corresponding extraordinary prisms and n_J is the number of extraordinary joints. In other words, there is one weight function for each extraordinary joint and several weight functions for each extraordinary prism. The construction of the prism weight functions $w_{k,\ell}^P(\mathbf{x})$ are introduced in Section 4.2.1 and the joint weight functions $w_\ell^J(\mathbf{x})$ in Section 4.2.2.

After the weight functions are determined, for blending we assign a tri-quadratic Bernstein basis $\mathbf{Q}(\mathbf{x})$ to each weight function. In the following, the domain of each tri-quadratic Bernstein basis $\mathbf{Q}(\mathbf{x})$ is assumed to be a cuboid enclosing the support of the corresponding weight function it is assigned to. We index the Bernstein basis similarly to the associated weight functions. Hence, similar to 1D and 2D, the SB-splines are defined by

$$\mathbf{N}(\mathbf{x}) = \begin{pmatrix} w^B(\mathbf{x}) \mathbf{B}(\mathbf{x})^\top & w_{1,1}^P(\mathbf{x}) \mathbf{Q}_{1,1}(\mathbf{x})^\top & \cdots & w_{n_p, n_{np}}^P(\mathbf{x}) \mathbf{Q}_{n_p, n_{np}}(\mathbf{x})^\top & w_1^J(\mathbf{x}) \mathbf{Q}_1(\mathbf{x})^\top & \cdots & w_{n_J}^J(\mathbf{x}) \mathbf{Q}_{n_J}(\mathbf{x})^\top \end{pmatrix}^\top. \quad (18)$$

4.2.1. Weight functions for extraordinary prisms

The weight functions for one extraordinary prism are obtained as illustrated in Figures 11 and 12. The two ends of the prism are either joined to an extraordinary joint or the boundary of the domain Ω . The centre of the prism consists of n_{ee} extraordinary edges of valence $e = 3$. For constructing the weight functions the prism is partitioned into e sectors, see Figure 11a. Each sector consists of $3 \times 3 \times n_{ee}$ elements and is parametrised using $\xi = (\xi_1, \xi_2, \xi_3) \in \hat{\Omega}$ with the parametric domain $\hat{\Omega} := [0, 1] \times [0, 1] \times [0, 1]$. The extraordinary edges are located along the parametric axis $\xi = (0, 0, \xi_3)$. The elements on $\hat{\Omega}$ are mapped to the reference element \square for integration using a mapping $\eta(\xi)$ composed of a translation, rotation and scaling.

On a given sector of the k -th prism, we define n_k univariate weight functions $w_{k,\ell}^{\text{II}}(\xi_3)$ from the available quadratic univariate B-splines $B_i(\xi_3)$. The number of weight functions n_k can be chosen flexibly, as long as

- each $w_{k,\ell}^{\text{II}}(\xi_3)$ is the sum of a certain number of consecutive B-splines,
- each $w_{k,\ell}^{\text{II}}(\xi_3)$ has vanishing derivatives at the endpoints of its support,
- each B-spline is used to build exactly one $w_{k,\ell}^{\text{II}}(\xi_3)$, c.f. Figure 11b,
- and the sum of all $w_{k,\ell}^{\text{II}}(\xi_3)$ is equal to 1.

For instance, in Figure 11b the univariate weight functions $w_{k,\ell}^{\text{II}}(\xi_3)$ are defined as

$$w_{k,1}^{\text{II}}(\xi_3) = \sum_{i=1}^4 B_i(\xi_3), \quad w_{k,2}^{\text{II}}(\xi_3) = \sum_{i=5}^8 B_i(\xi_3), \quad w_{k,3}^{\text{II}}(\xi_3) = \sum_{i=9}^{12} B_i(\xi_3). \quad (19)$$

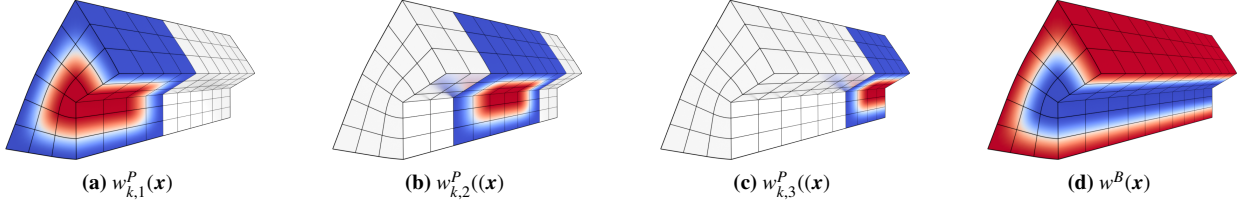


Figure 12: Weight functions for the extraordinary prism. The weight functions $w_{k,1}^P(x)$, $w_{k,2}^P(x)$ and $w_{k,3}^P(x)$ are obtained by choosing three univariate weight functions $w_{k,1}^{\text{II}}(\xi_3)$, $w_{k,2}^{\text{II}}(\xi_3)$ and $w_{k,3}^{\text{II}}(\xi_3)$ along the centre of the extraordinary prism as depicted in Figure 11b. The weight function $w^B(x)$ is their complement to one, i.e. $w^B(x) = 1 - w_{k,1}^P(x) - w_{k,2}^P(x) - w_{k,3}^P(x)$. The scalar field ranges between 0 (blue) and 1 (red).

The isocontours of the three weight functions and their complement to one $w^B(x)$ on two of the three sectors are depicted in Figure 12. Note that choosing a large n_k ensures that the SB-splines have small support sizes.

Following the above, the trivariate weight functions $w_{k,\ell}^P(\xi_1, \xi_2, \xi_3)$ are defined as the tensor product of the bivariate weight function $w^I(\xi_1) \otimes w^I(\xi_2)$, introduced in Section 3.2.1, and the n_k univariate weight functions $w_{k,\ell}^{\text{II}}(\xi_3)$,

$$w_{k,\ell}^P(\xi) = w^I(\xi_1) \otimes w^I(\xi_2) \otimes w_{k,\ell}^{\text{II}}(\xi_3), \quad \ell = 1, \dots, n_k. \quad (20)$$

The construction is repeated for all prisms to obtain weight functions for all k .

4.2.2. Weight functions for extraordinary joints

Without loss of generality, we consider a single extraordinary joint with valence $v = 4$ shared by four extraordinary prisms each of which have valence $e = 3$, see Figure 9, and describe the construction of its associated weight function. To simplify the construction of the extraordinary joint weight function $w_\ell^J(x)$ we require that the support of the already defined prism weight functions $w_{k,\ell}^P(x)$ do not overlap at the joint. Recall from the Figures 11 and 12 that the support of the prism weight functions $w_{k,\ell}^P(x)$ consist in the $\xi_1 \xi_2$ -plane corresponds to the 3-neighbourhood of the extraordinary vertex. Hence, we choose the 3-neighbourhood of the extraordinary vertex at the centre of the joint for constructing the weight function $w_\ell^J(x)$ as illustrated in Figure 13a. At the boundary of the 3-neighbourhood, the joint meets different prisms; the intersection of the joint with each prism is composed of $3 \times 3 \times e$ quadrilateral faces, with e the valence of the prism's extraordinary edge. We require that across this $3 \times 3 \times e$ of faces, the values and derivatives of the weight function $w_\ell^J(x)$ respectively match those of the unique prism weight function that is non-zero on all these faces. For instance, in the already discussed example in Figure 11b the weight functions $w_{k,1}^P(x)$ and $w_{k,3}^P(x)$ corresponding to $w_{k,1}^{\text{II}}(\xi_3)$ and $w_{k,3}^{\text{II}}(\xi_3)$ have to smoothly connect to the respective joint weight functions.

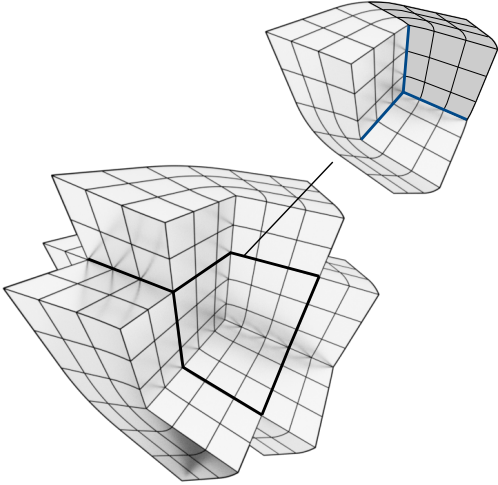
To construct the joint weight function $w_\ell^J(x)$ we follow once more a sector-wise approach as outlined in Figure 13. The joint is partitioned into $v = 4$ sectors each consisting of $3 \times 3 \times 3$ elements. Each sector is parametrised using $\xi = (\xi_1, \xi_2, \xi_3) \in \hat{\Omega}$ on the parametric domain $\hat{\Omega} := [0, 1] \times [0, 1] \times [0, 1]$. The extraordinary edges of the attached four prisms meet at the origin $\xi = (0, 0, 0)$ of the domain $\hat{\Omega}$. We define the joint weight function $w_\ell^J(\xi)$ as

$$w_\ell^J(\xi) = 1 - w^{\text{III}}(\xi_1) \otimes w^{\text{III}}(\xi_2) \otimes w^{\text{III}}(\xi_3) - (1 - w^{\text{III}}(\xi_1)) \otimes w^{\text{III}}(\xi_2) \otimes w^{\text{III}}(\xi_3) \\ - w^{\text{III}}(\xi_1) \otimes (1 - w^{\text{III}}(\xi_2)) \otimes w^{\text{III}}(\xi_3) - w^{\text{III}}(\xi_1) \otimes w^{\text{III}}(\xi_2) \otimes (1 - w^{\text{III}}(\xi_3)), \quad (21)$$

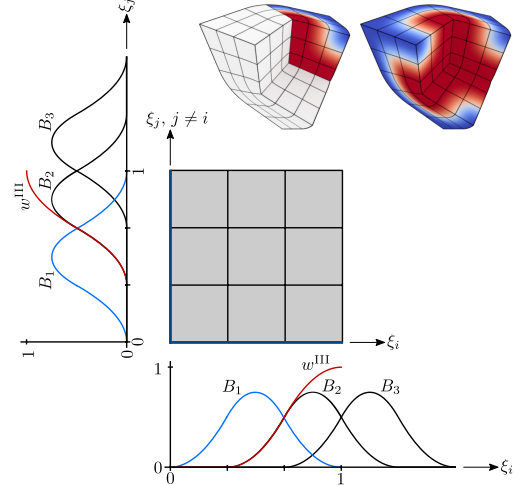
where the univariate weight functions $w^{\text{III}}(\xi_i)$ are, as depicted in Figure 13b, assembled from the smooth quadratic B-splines defined along the ξ_1 , ξ_2 or ξ_3 axes. That is,

$$w^{\text{III}}(\xi_i) = B_2(\xi_i) + B_3(\xi_i) \quad i = 1, 2, 3. \quad (22)$$

In Figure 14 the isocontours of the obtained joint weight function $w_\ell^J(x)$, the weight functions $w_{k,\ell}^P(x)$ of the attached four prisms and their complement to one $w^B(x)$ are shown. In Appendix D we briefly demonstrate that the joint and prism weight functions for arbitrary vertex and edge valences v and e can be constructed following same approach.



(a) Extraordinary joint and the attached prisms with some elements not shown



(b) Univariate weight functions in red and univariate B-splines in black and blue

Figure 13: Construction of the extraordinary joint weight function $w_\ell^J(\mathbf{x})$ on one of the $v = 4$ sectors. Each sector consists of the $3 \times 3 \times 3$ elements shown in (a). The weight function $w_\ell^J(\xi)$ is obtained using the univariate weight functions $w^{III}(\xi_1)$, $w^{III}(\xi_2)$ and $w^{III}(\xi_3)$ shown in (b) which are simply the complement to ones of $w^I(\xi_i) = 1 - w^{III}(\xi_i)$ with $i = 1, 2, 3$ shown earlier in Figure 11b. The result is shown at the top right of (b) with the scalar field ranging between 0 (blue) and 1 (red).

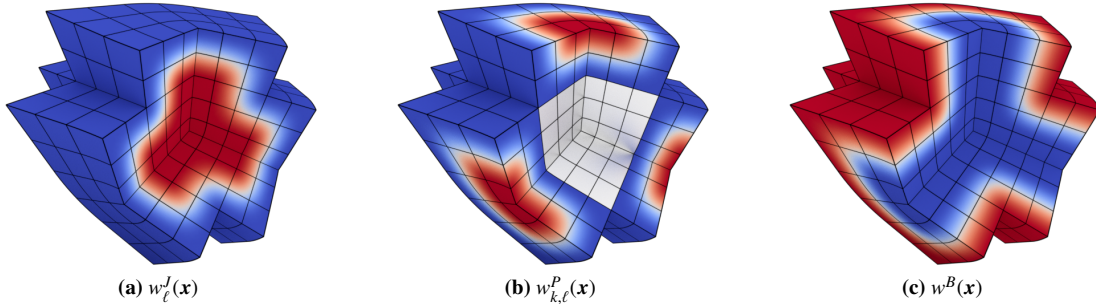


Figure 14: Extraordinary joint weight function $w_\ell^J(\mathbf{x})$, extraordinary prism weight functions $w_{k,\ell}^P(\mathbf{x})$ and their complement to one $w^B(\mathbf{x})$. The scalar field ranges between 0 (blue) and 1 (red).

5. Examples

5.1. One-dimensional Poisson problem

As a first example we consider the solution of a one-dimensional Poisson-Dirichlet problem $-\frac{d^2u}{dx^2} = f$ on the domain $\Omega = (0, 1)$. The body force $f(x)$ is chosen such that the solution is

$$u(x) = \sin(3\pi x). \quad (23)$$

The domain is parametrised using non-uniform B-splines of degree $p_B = 2$ and $p_B = 3$ in turn. The knot vector and control points x_i are selected so that each element has the same size h . We intentionally introduce a C^0 continuous kink at the midspan $x = 1/2$ by setting the knot multiplicity to p_B therein. In addition, we use an open knot vector which allows the Dirichlet boundary condition to be imposed strongly.

In the following we compare the finite element convergence between the B-splines $\mathbf{B}(x)$, consisting of C^0 and C^{p_B-1} continuous basis functions, and the SB-splines $N(x)$. The C^1 continuous SB-splines $N(x)$ are constructed by blending

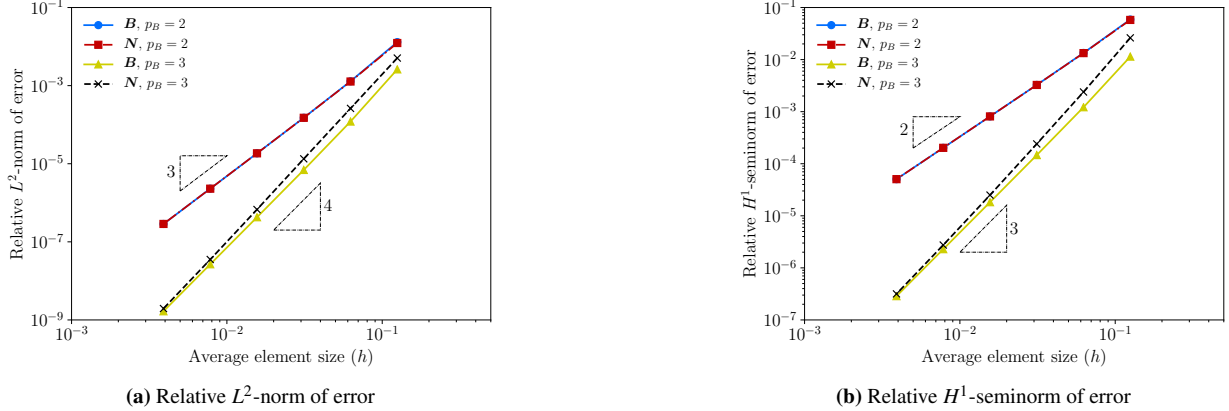


Figure 15: One-dimensional Poisson-Dirichlet problem. Comparison of convergence between the B-splines $\mathbf{B}(x)$, consisting of C^0 and C^{p_B-1} continuous basis functions, and the C^1 continuous SB-splines $N(x)$.

B-splines $\mathbf{B}(x)$ with Bernstein basis $\mathbf{Q}(x)$ of same polynomial degree $p_Q = p_B$. In comparison to B-splines $\mathbf{B}(x)$, for the SB-splines $N(x)$ the additional degrees of freedom are $n_Q = p_Q + 1$. We begin with an initial coarse mesh of $n_e = 8$ elements and obtain finer meshes using knot insertion. Figure 15 shows that the SB-splines $N(x)$ yield an optimal convergence rate for both polynomial degrees $p_B = 2$ and $p_B = 3$. Besides that, the approximation error remains in the same order of magnitude with or without blending.

5.2. Poisson and biharmonic problems on a square domain

We consider next the Poisson-Dirichlet and biharmonic problems on a square domain $\Omega = (0, 1) \times (0, 1)$. Figure 16 shows the initial coarse mesh of the square domain with 8 extraordinary vertices. The boundary of the square domain is parametrised using open, uniform bi-quadratic B-splines. For the Poisson-Dirichlet problem, the Dirichlet boundary condition is imposed using Nitsche's method with the stabilisation parameter chosen as $\gamma = 10/h^2$, see Appendix B. For the biharmonic problem, we use the penalty approach with the stabilisation parameter chosen as $\gamma = 1/h^2$. In comparison to mixed B-splines $\mathbf{B}(x)$, for the SB-splines $N(x)$ the additional degrees of freedom are $n_Q = 8 \times 9 = 72$. We refine the mesh using a refinement scheme described in Appendix C.

We approximate the finite element integrals using the Gauss-Legendre quadrature rule. In order to examine the effect of the number of quadrature points n_{gp} on the finite element convergence, for the SB-splines $N(x)$, we vary n_{gp} for the domain integrals and use 3 quadrature points for the boundary integrals. For the mixed B-splines $\mathbf{B}(x)$, we use for the domain integrals and boundary integrals 3×3 and 3 quadrature points, respectively.

For the two-dimensional Poisson-Dirichlet problem, the body force $f(\mathbf{x})$ is chosen so that the solution is

$$u(\mathbf{x}) = \sin(6x_1) \sin(8x_2). \quad (24)$$

Figure 17 shows that the SB-splines are optimally convergent provided that at least $n_{gp} = 3 \times 3$ quadrature points are used. For $n_{gp} = 3 \times 3$, as the mesh is refined the approximation error remains in the same order of magnitude with or without blending. We believe that the number of quadrature points n_{gp} for the SB-splines $N(x)$ to achieve the optimal convergence rate is relatively small because the weight functions $w^B(\mathbf{x})$ and $w^Q(\mathbf{x})$ are assembled from smooth piecewise quadratic B-splines. For the two-dimensional biharmonic problem, the body force $f(\mathbf{x})$ is chosen so that the solution is equal to

$$u(\mathbf{x}) = \frac{\sin(\pi x_1) \sin(\pi x_2)}{4\pi^2}. \quad (25)$$

As the mixed B-splines $\mathbf{B}(x)$ are not globally C^1 continuous, here we examine only the finite element convergence using the C^1 continuous SB-splines $N(x)$. Figure 18 shows that the SB-splines $N(x)$ are optimally convergent for the biharmonic problem provided that a minimum of $n_{gp} = 2 \times 2$ is used for the quadrature. However, note that the

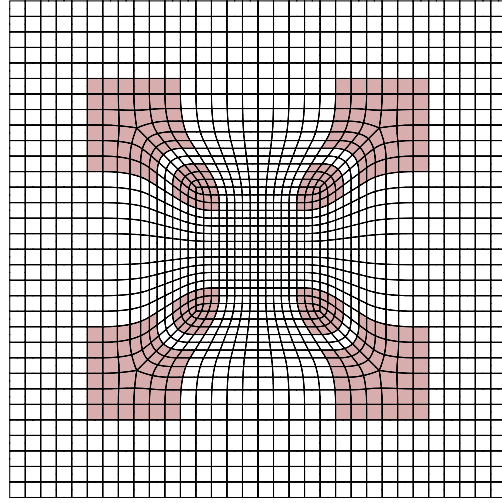


Figure 16: Initial coarse mesh of the square domain. The blending domain Ω_Q for the initial coarse mesh is shaded in pink.

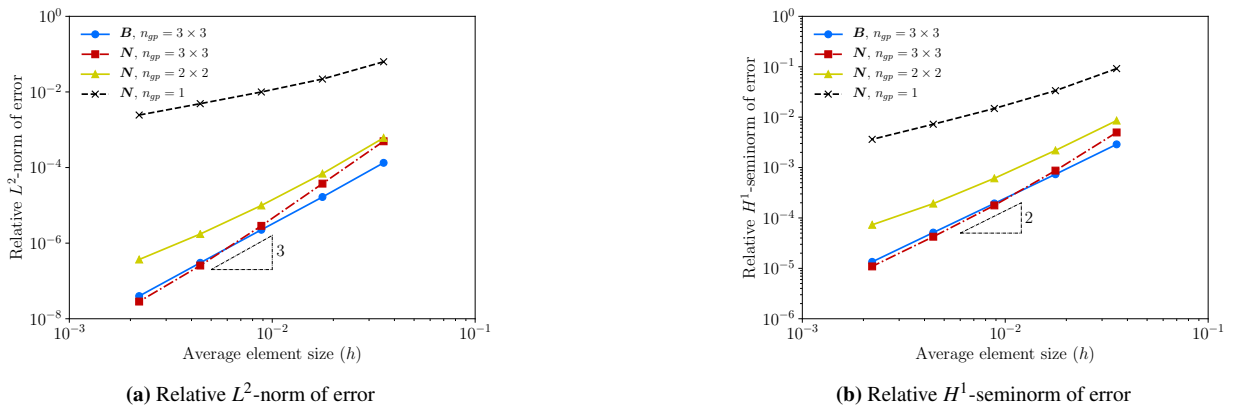


Figure 17: Poisson-Dirichlet problem on a square domain. Convergence with mixed B-splines $\mathbf{B}(\mathbf{x})$ and SB-splines $\mathbf{N}(\mathbf{x})$.

relative H^2 -seminorm of error is improved using $n_{gp} = 3 \times 3$. In addition to the convergence rate, we examine the finite element solution $u^h(\mathbf{x})$ for the biharmonic problem qualitatively. Figure 19 shows the finite element solution $u^h(\mathbf{x})$ and its first and second partial derivatives with respect to x_1 for the initial coarse mesh. Since the SB-splines $\mathbf{N}(\mathbf{x})$ are globally C^1 continuous, both the finite element solution $u^h(\mathbf{x})$ and its first partial derivative with respect to x_1 are continuous as visible in Figures 19a and 19b, respectively. Furthermore, as known the spatial derivatives of $u^h(\mathbf{x})$ often exhibit short-wavelength oscillations near the extraordinary vertices. Similarly, we observe such oscillations specifically for the second spatial derivatives in the blending domain Ω_Q as shown in Figure 19c. However, there is no oscillation in the 1-neighbourhood of the extraordinary vertices.

5.3. Biharmonic problem on v -gon domains

In some smooth basis function construction techniques, the respective finite element convergence rates are known to deteriorate when the valence v is increased, see the discussion in [29]. Therefore, we investigate next the convergence rate of the SB-splines $\mathbf{N}(\mathbf{x})$ for different valences. To this end, we consider the biharmonic problem on five v -gon domains with $v \in \{3, 5, 6, 7, 8\}$ as depicted in Figure 20. For each domain, the extraordinary vertex is located at the global origin $\mathbf{x} = (0 \ 0)^\top$. The boundary is parametrised with open, uniform bi-quadratic B-splines. To impose the boundary conditions, we use the penalty approach with the stabilisation parameter chosen as $\gamma = 1000/h^2$.

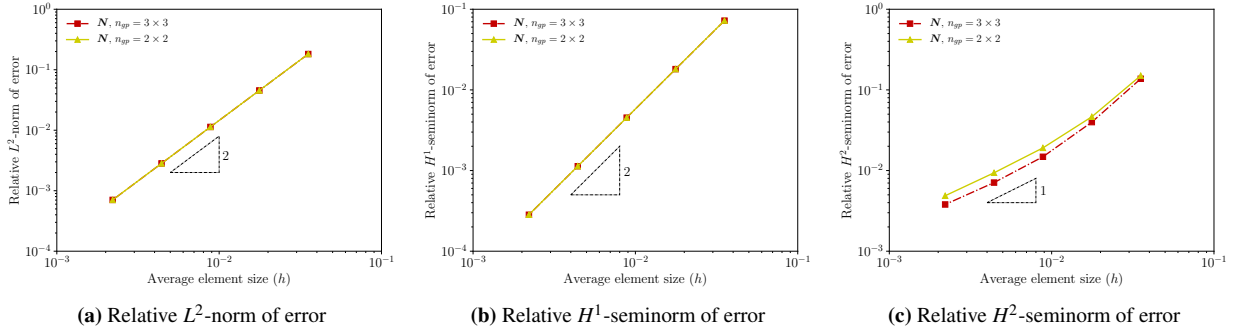


Figure 18: Biharmonic problem on a square domain. Convergence with SB-splines $N(\mathbf{x})$.

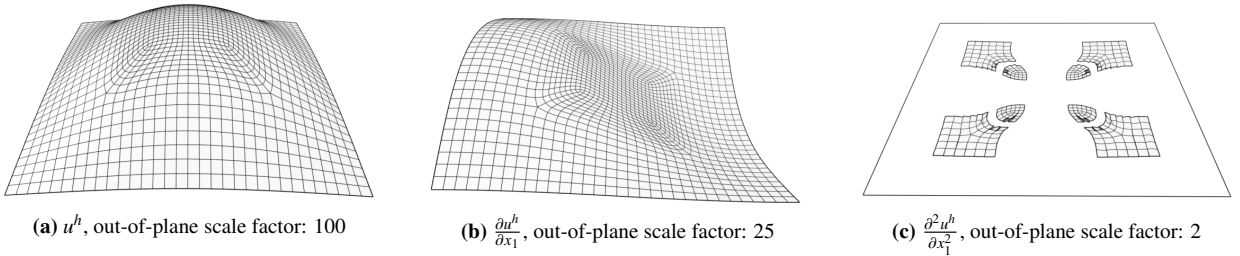


Figure 19: Biharmonic problem on a square domain. The finite element solution u^h and its first and second partial derivatives with respect to x_1 for the initial coarse mesh. All plots have been warped in the out-of-plane direction using the stated scale factors. In (a) and (b) all elements are shown whereas in (c) only elements in the blending domain Ω_Q are shown.

As shown to be sufficient for the biharmonic problem in Section 5.2, we use 3×3 and 3 quadrature points for approximating the domain and boundary integrals, respectively. Similarly, we refine the mesh using the refinement scheme described in Appendix C. The body force $f(\mathbf{x})$ is chosen such that the solution is

$$u(\mathbf{x}) = \sin(3x_1) \cos(3x_2). \quad (26)$$

Figure 21 shows the finite element convergence using the SB-splines $N(\mathbf{x})$. Although the convergence rates for the first few coarser meshes are slightly fluctuating, overall the SB-splines $N(\mathbf{x})$ are optimally convergent. In other words, the convergence rate is identical for the considered valences $v \in \{3, 5, 6, 7, 8\}$. The increase of the valence leads, however, to a small increase in the convergence constants. This finding suggests that the SB-splines $N(\mathbf{x})$ are robust since the studied valences $v \in \{3, 5, 6, 7, 8\}$ are the most prevalent in well-designed meshes.

5.4. Poisson and biharmonic problems on a spherical domain

As a final example, we consider the Poisson-Dirichlet and biharmonic problems on the spherical domain in Figure 1. The spherical domain has a radius of 2.55 and is centred at the global origin $\mathbf{x} = (0, 0, 0)$. As an approximation to the spherical domain, the parametrised hexahedral mesh in Figure 1b has an average mesh size $h = 0.4228$ and consists of 20 extraordinary prisms of valence $e = 3$ and 8 extraordinary joints. The boundary of the spherical domain is parametrised using open, uniform tri-quadratic B-splines. For the Poisson-Dirichlet problem, the Dirichlet boundary condition is imposed using Nitsche's method with the stabilisation parameter chosen as $\gamma = 10/h^2$. For the biharmonic problem, we use the penalty approach with the stabilisation parameter chosen as $\gamma = 1000/h^2$. The numbers of degrees of freedom for the mixed B-splines $\mathbf{B}(\mathbf{x})$ and the SB-splines $N(\mathbf{x})$ are 6413 and $6413 + (20 + 8) \times 27 = 7169$, respectively.

For the three-dimensional Poisson-Dirichlet problem, the body force $f(\mathbf{x})$ is chosen so that the solution is

$$u(\mathbf{x}) = \sin\left(\frac{x_1}{2}\right) \sin\left(\frac{x_2}{2}\right) \sin\left(\frac{x_3}{4}\right). \quad (27)$$

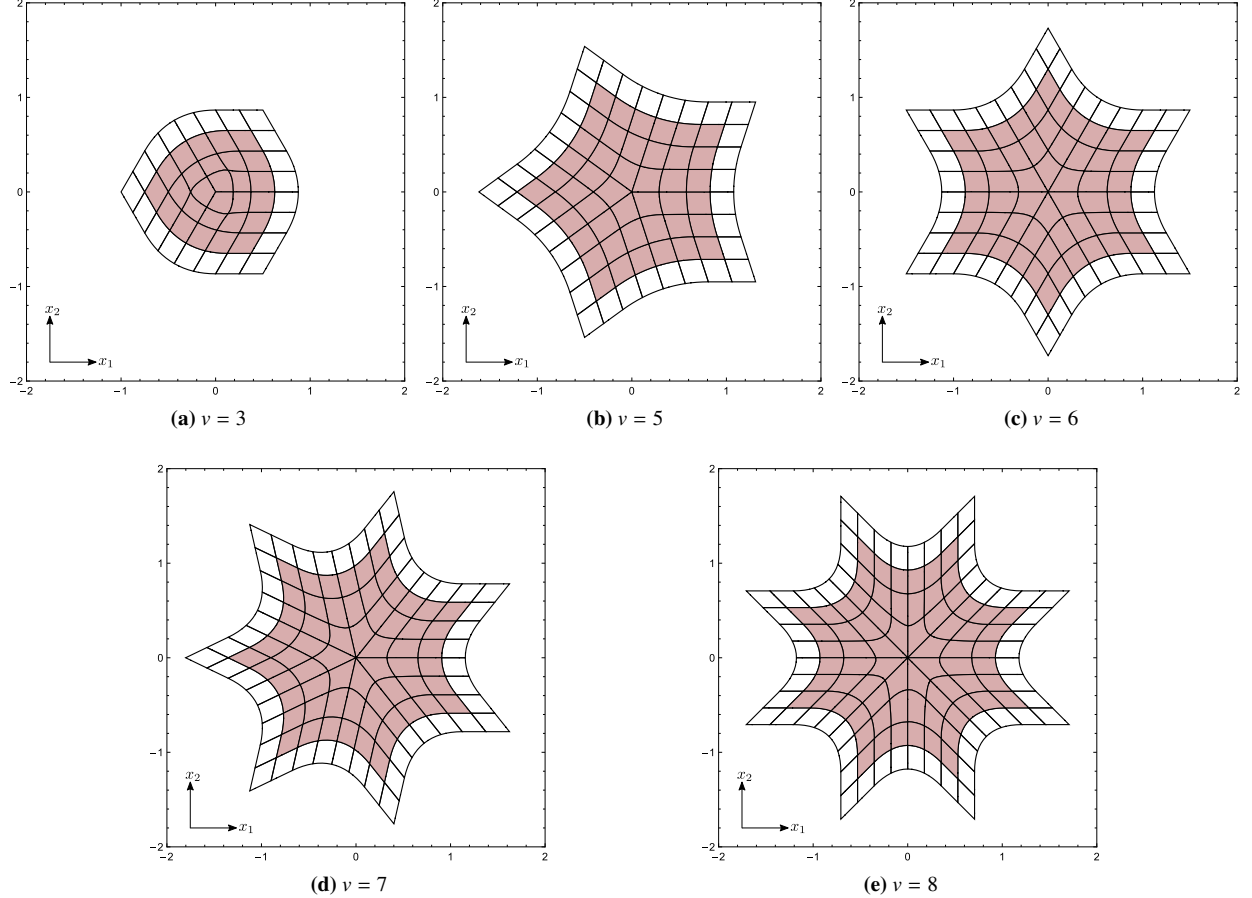


Figure 20: Initial coarse meshes for the v -gon domains. For each initial coarse mesh the blending domain Ω_Q is shaded in pink.

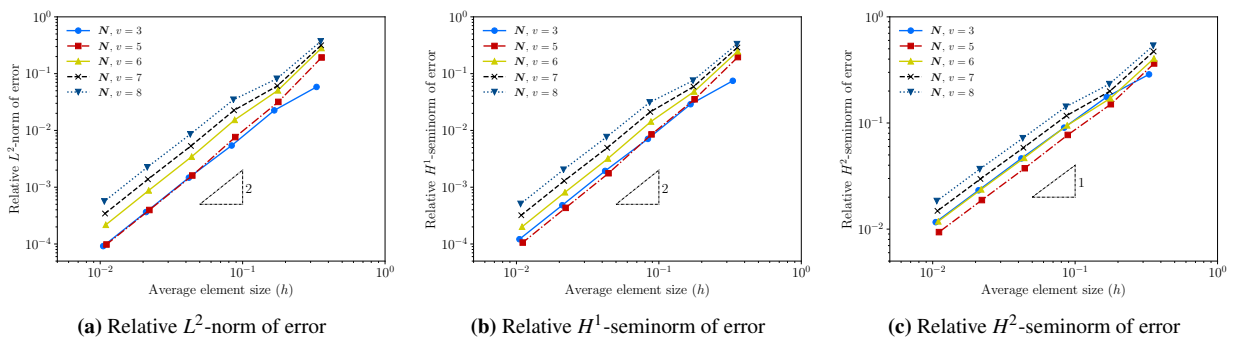


Figure 21: Biharmonic problem on v -gon domains. Convergence with SB-splines $N(x)$.

We compare numerically the finite element solution $u^h(\mathbf{x})$ between $\mathbf{B}(\mathbf{x})$ and $\mathbf{N}(\mathbf{x})$. The relative L^2 -norms of error for $\mathbf{B}(\mathbf{x})$ and $\mathbf{N}(\mathbf{x})$ are 4.9111×10^{-4} and 3.9034×10^{-4} , respectively whereas the relative H^1 -seminorms of error for $\mathbf{B}(\mathbf{x})$ and $\mathbf{N}(\mathbf{x})$ are 5.1337×10^{-3} and 3.5630×10^{-3} , respectively. Therefore, the approximation error has the same order of magnitude with and without blending. Figure 22 illustrates the first partial derivative of the finite element solution with respect to x_1 . As shown in the figure, both $\mathbf{B}(\mathbf{x})$ and $\mathbf{N}(\mathbf{x})$ yield an accurate approximation to the first partial derivative of the analytical solution with respect to x_1 . In addition, Figure 23 ascertains that the SB-splines $\mathbf{N}(\mathbf{x})$ are globally C^1 continuous. For instance, the mixed B-splines $\mathbf{B}(\mathbf{x})$ yield C^0 continuous finite element solution $u^h(\mathbf{x})$ near the extraordinary edges as inferred from the discontinuity of the first partial derivative of u^h with respect to x_1 in Figure 23a. In contrast, the first partial derivative of u^h with respect to x_1 using $\mathbf{N}(\mathbf{x})$ is continuous in the same subdomains as shown in Figure 23b.

For the three-dimensional biharmonic problem, the body force $f(\mathbf{x})$ is chosen so that the solution is equal to

$$u(\mathbf{x}) = \frac{1}{8\pi} \sin\left(\frac{\pi x_1}{8}\right) \sin\left(\frac{\pi x_2}{8}\right) \sin\left(\frac{\pi x_3}{8}\right). \quad (28)$$

Using the SB-splines $\mathbf{N}(\mathbf{x})$, the relative L^2 -norm of error, relative H^1 -seminorm of error and relative H^2 -seminorm of error are 9.8943×10^{-4} , 3.7825×10^{-3} and 6.4669×10^{-2} , respectively. Figure 24 shows that the SB-splines $\mathbf{N}(\mathbf{x})$ yield a satisfactory finite element approximation to the analytical solution.

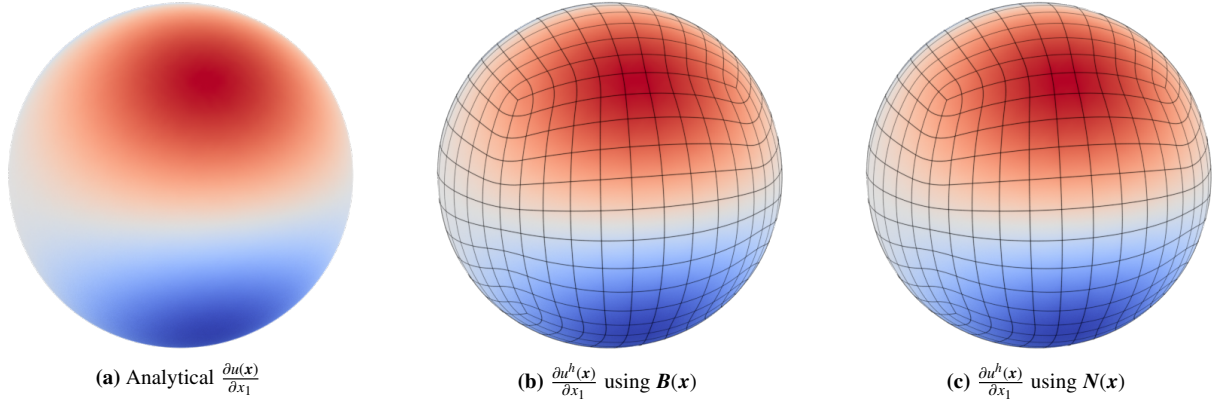


Figure 22: Poisson-Dirichlet problem on a spherical domain. Isocontours of the first partial derivative of the field solution with respect to x_1 on the spline surface. The scalar field ranges between -0.18 (blue) and 0.18 (red).

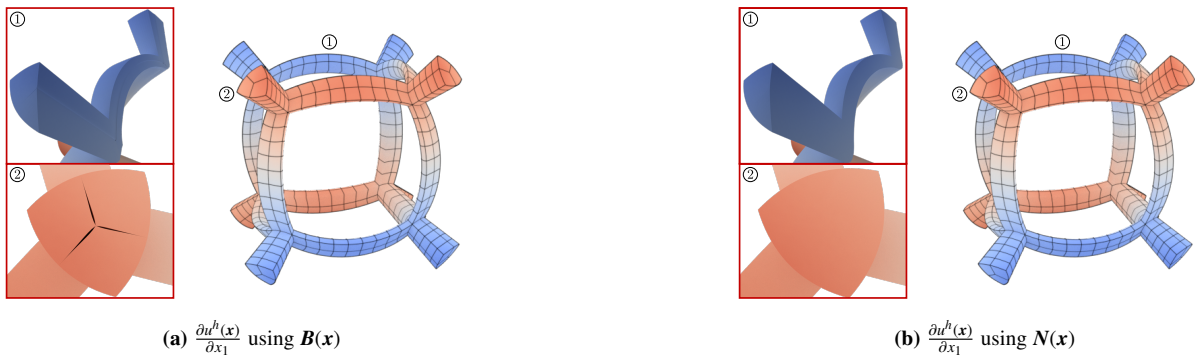


Figure 23: Poisson-Dirichlet problem on a spherical domain. Isocontours of the first partial derivative of the finite element solution with respect to x_1 near the extraordinary edges. For consistency, the scalar field herein has the same scale as Figure 22.

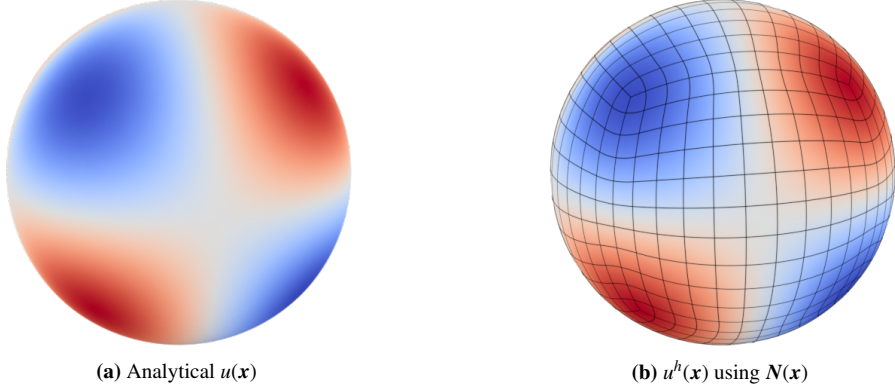


Figure 24: Biharmonic problem on a spherical domain. Isocontours of the field solution on the spline surface. The scalar field ranges between -0.43 (blue) and 0.43 (red).

6. Conclusions

We introduced SB-splines i.e. a smooth blended B-spline construction for unstructured quadrilateral and hexahedral meshes and demonstrated its optimal convergence for quadratic B-splines on unstructured quadrilateral and hexahedral meshes. We determine the smooth weight functions required for blending from the smooth mixed B-splines defined on the regular parts of the unstructured mesh. The weight functions multiplied with the available mixed B-splines and additionally introduced Bernstein basis functions yield new basis functions. As shown numerically, the SB-splines can be efficiently integrated using standard Gauss-Legendre quadrature with a very small number of quadrature points. In the blending region, the new basis functions have slightly larger support close to the extraordinary features. For instance, in 2D the support consists of the 3-neighbourhood of the extraordinary vertex. Remarkably, the numerically determined convergence rates in 2D are optimal for both Poisson and biharmonic problems and are independent of the valence of the extraordinary vertex. However, the convergence constants show a slight increase with an increase in valence, which may be explained by the short-wavelength oscillations, or ripples, in the higher-order derivatives at the blending region. As discussed, on unstructured hexahedral meshes, the extraordinary edges and vertices usually form a connected network. The respective weight functions obtained from the available smooth mixed B-splines may not have a compact support. Therefore, we decompose the weight functions so that the resulting weight functions and basis functions have a compact support and are still polynomials in the parameter space.

In closing, we stress that the proposed construction can be applied to mixed B-splines of arbitrary degrees, although we have studied only quadratic mixed B-splines so far. To this end, it is necessary to extend the introduced mesh refinement scheme for quadratic mixed B-splines to arbitrary degree. In our experience, the details of this refinement are important for achieving optimal convergence rates. For cubic SB-splines the mixed $C^0/C^1/C^2$ B-splines introduced in Wei et al. [53] appear as particularly promising. Moreover, while we presented some mathematical analyses (e.g., proof of linear independence in 1D), further analysis is needed to prove the numerically observed properties of SB-splines. In principle, the proposed construction can also be applied to non-uniform B-splines. Non-uniform constructions can, amongst others, significantly simplify the enforcement of essential boundary conditions. Lastly, to make the presented construction useful in geometric design, the introduced new degrees of freedom around the extraordinary features must be associated with control vertex positions. This may be achieved by projecting the new degrees of freedom to the existing or possibly some new control vertex positions in the mesh.

Appendix A. Linear independence

We provide in this appendix a proof for the linear independence of the one-dimensional SB-splines. We consider as in Figures 2 and 3 a 1D setup with n_B mixed B-splines $B_i(x)$ of degree $p_B \geq 2$. As discussed in Section 2, we assume that the prescribed B-spline smoothness is C^0 at a single breakpoint and C^{p_B-1} at all others. In general, the

mixed B-splines $B_i(x)$ will be non-polynomials in physical space because of the isoparametric mapping, see (2). Let \mathcal{B} denote the set of n_B mixed B-splines $B_i(x)$, \mathcal{P} the set of $n_Q = p_Q + 1$ Bernstein polynomials and \mathcal{N} the set of $n_N = n_B + n_Q$ SB-splines. The set \mathcal{B} is split into the two non-intersecting sets

$$\mathcal{B}^B = \{B_i \mid \text{supp } B_i \subset \Omega^Q\} \quad \text{and} \quad \mathcal{B}^C = \mathcal{B} \setminus \mathcal{B}^B. \quad (\text{A.1})$$

The set \mathcal{N} is composed of the three non-intersecting sets

$$\mathcal{N}^B = \{w^B B_i \mid B_i \in \mathcal{B}^B\}, \quad \mathcal{N}^Q = \{w^Q Q_i \mid Q_i \in \mathcal{P}\} \quad \text{and} \quad \mathcal{N}^C = \mathcal{N} \setminus (\mathcal{N}^B \cup \mathcal{N}^Q). \quad (\text{A.2})$$

As implied by the choice of weight function in (6), $\#B_i \in \mathcal{B}^B$ such that $w^B|_{\text{supp } B_i} = 0$, and similarly $\#Q_i \in \mathcal{P}$ such that $w^Q|_{\text{supp } Q_i} = 0$. We want to prove that the functions in \mathcal{N} are linearly independent.

Linear independence requires that

$$\sum_{N_i \in \mathcal{N}} N_i(x) \alpha_i = 0 \quad \forall x \in \Omega, \quad (\text{A.3})$$

is satisfied only when the coefficients $\alpha_i = 0$. Observe that outside the blending domain, (A.3) reduces to

$$\sum_{N_i \in \mathcal{N}^C} N_i(x) \alpha_i = \sum_{B_i \in \mathcal{B}^C} B_i(x) \alpha_i = 0 \quad \forall x \in \Omega \setminus \Omega^Q. \quad (\text{A.4})$$

Therefore, due to the linear independence of B-splines, we obtain $\alpha_i = 0$ for all $N_i(x) \in \mathcal{N}^C$. The remaining terms in (A.3) correspond to splines with a support inside the blending region Ω^Q . We prove by contradiction that the coefficients of the non-vanishing terms must be zeros. Assume that the SB-splines are linearly dependent such that

$$\sum_{N_i \in \mathcal{N}^B} N_i(x) \alpha_i = \sum_{N_j \in \mathcal{N}^Q} N_j(x) \alpha_j \quad \forall x \in \Omega^Q, \quad (\text{A.5})$$

or equivalently that

$$w^B(x) \sum_{B_i \in \mathcal{B}^B} B_i(x) \alpha_i = (1 - w^B(x)) \sum_{Q_j \in \mathcal{P}} Q_j(x) \alpha_j. \quad (\text{A.6})$$

Next, observe that there are two elements $\Omega_{k1}, \Omega_{k2} \subset \Omega^Q$ such that on each there is only one function from \mathcal{N}^B that is non-zero, e.g., the leftmost or the rightmost element in the grey region in Figure 2 or Figure 3. Let the corresponding non-zero functions be N_{i1}, N_{i2} , respectively. Then, we have $w^B|_{\Omega_{k\ell}} = (1 - B_{i\ell})$ and $w^Q|_{\Omega_{k\ell}} = B_{i\ell}$, $\ell = 1, 2$, thus

$$(1 - B_{i\ell}(x)) \alpha_{i\ell} = \sum_{Q_j \in \mathcal{P}} Q_j(x) \alpha_j \quad \forall x \in \Omega_{k\ell} \subset \Omega^Q, \quad \ell = 1, 2. \quad (\text{A.7})$$

Note that the right hand side is a polynomial function.

- Case 1: Let $B_{i\ell}|_{\Omega_{k\ell}}$ be non-polynomial. Then, the equality in (A.7) can be satisfied only if both sides are equal to 0.
- Case 2: Let the isoparametric mapping be such that both Ω_{k1}, Ω_{k2} are obtained by affinely mapping the associated element in parameter space. Thus, $B_{i\ell}|_{\Omega_{k\ell}}$ are degree p_B polynomials for both $\ell = 1, 2$. This has two implications. First, for equality, both the left and right hand sides in (A.7) need to represent the same polynomial, say f , of degree $p = \min\{p_B, p_Q\}$. Note that f is thus a global polynomial on Ω^Q . Second, by the end-point vanishing property of B-splines, $B_{i\ell}$ vanishes p_B times on one of the endpoints of $\Omega_{k\ell}$, $\ell = 1, 2$. This imposes $2p_B$ constraints on the polynomial f , thus implying $f = 0$.

Both the above cases imply that the right hand side in (A.7) is zero and, in particular, all coefficients of Q_i are thus zero by their linear independence. As a result, the right hand side in (A.6) is zero, thus implying that all coefficients of $B_i \in \mathcal{B}^B$ are zero by their linear independence.

Appendix B. Finite element discretisation

Appendix B.1. Poisson equation

The Poisson equation is given by

$$\begin{aligned} -\Delta u &= f && \text{in } \Omega, \\ u &= \bar{u} && \text{on } \Gamma_D, \\ \nabla u \cdot \mathbf{n} &= \bar{t} && \text{on } \Gamma_N, \end{aligned} \tag{B.1}$$

where u is the solution field in the domain Ω due to the body force f , \bar{u} is the prescribed solution field on the Dirichlet boundary Γ_D , \bar{t} is the prescribed flux on the Neumann boundary Γ_N with the outward unit normal \mathbf{n} , ∇ is the gradient operator and $\Delta = \nabla \cdot \nabla$ is the Laplacian operator. The weak formulation of the Poisson equation can be stated as [60, 61]: Find $u \in H^1(\Omega)$ such that

$$a(u, v) = l(v), \tag{B.2}$$

for all $v \in H^1(\Omega)$ with

$$a(u, v) = \int_{\Omega} \nabla u \cdot \nabla v \, d\Omega + \gamma \int_{\Gamma_D} uv \, d\Gamma - \int_{\Gamma_D} (u(\nabla v \cdot \mathbf{n}) + v(\nabla u \cdot \mathbf{n})) \, d\Gamma, \tag{B.3a}$$

$$l(v) = \int_{\Omega} vs \, d\Omega + \int_{\Gamma_N} v\bar{t} \, d\Gamma + \gamma \int_{\Gamma_D} v\bar{u} \, d\Gamma - \int_{\Gamma_D} (\nabla v \cdot \mathbf{n})\bar{u} \, d\Gamma, \tag{B.3b}$$

and the positive stabilisation parameter γ .

Appendix B.2. Biharmonic equation

The biharmonic equation is given by

$$\begin{aligned} \Delta^2 u &= f && \text{in } \Omega, \\ u &= \bar{u}, \quad \nabla u \cdot \mathbf{n} = \bar{t} && \text{on } \Gamma_D, \\ \Delta u &= \bar{\kappa}, \quad \nabla(\Delta u) \cdot \mathbf{n} = \bar{\lambda} && \text{on } \Gamma_N, \end{aligned} \tag{B.4}$$

where $\bar{\kappa}$ and $\bar{\lambda}$ are respectively the bending moment and shear force prescribed on the Neumann boundary Γ_N . The weak formulation of the biharmonic equation can be stated as [62]: Find $u \in H^2(\Omega)$ such that

$$a(u, v) = l(v), \tag{B.5}$$

for all $v \in H^2(\Omega)$ where

$$\begin{aligned} a(u, v) &= \int_{\Omega} \Delta u \Delta v \, d\Omega + \gamma \int_{\Gamma_D} uv \, d\Gamma + \tau \int_{\Gamma_D} (\nabla u \cdot \mathbf{n})(\nabla v \cdot \mathbf{n}) \, d\Gamma + \int_{\Gamma_D} (u(\nabla(\Delta v) \cdot \mathbf{n}) + v(\nabla(\Delta u) \cdot \mathbf{n})) \, d\Gamma \\ &\quad - \int_{\Gamma_D} (\Delta u(\nabla v \cdot \mathbf{n}) + \Delta v(\nabla u \cdot \mathbf{n})) \, d\Gamma, \end{aligned} \tag{B.6a}$$

$$\begin{aligned} l(v) &= \int_{\Omega} vs \, d\Omega - \int_{\Gamma_N} v\bar{\lambda} \, d\Gamma + \int_{\Gamma_N} (\nabla v \cdot \mathbf{n})\bar{\kappa} \, d\Gamma + \gamma \int_{\Gamma_D} v\bar{u} \, d\Gamma + \tau \int_{\Gamma_D} (\nabla v \cdot \mathbf{n})\bar{t} \, d\Gamma \\ &\quad + \int_{\Gamma_D} (\nabla(\Delta v) \cdot \mathbf{n})\bar{u} \, d\Gamma - \int_{\Gamma_D} (\Delta v)\bar{t} \, d\Gamma. \end{aligned} \tag{B.6b}$$

Appendix B.3. Finite element discretisation

We discretise the trial and test functions with the SB-splines as

$$u^h(\mathbf{x}) = \sum_{i=1}^{n_N} N_i(\mathbf{x}) \alpha_i \quad \text{and} \quad v^h(\mathbf{x}) = \sum_{i=1}^{n_N} N_i(\mathbf{x}) \beta_i. \quad (\text{B.7})$$

Introducing the interpolation equation (B.7) into the weak form of Poisson equation (B.2) or biharmonic equation (B.5) yields a system of linear equations with the unknowns α_i . For instance, the bilinear form $a(u^h, v^h)$ for the Poisson equation becomes after discretisation

$$a(u^h, v^h) = \sum_{i=1}^{n_N} \sum_{j=1}^{n_N} \alpha_i \left(\int_{\Omega} \nabla N_i \nabla N_j \, d\Omega + \gamma \int_{\Gamma_D} N_i N_j \, d\Gamma - \int_{\Gamma_D} (N_i (\nabla N_j \cdot \mathbf{n}) + N_j (\nabla N_i \cdot \mathbf{n})) \, d\Gamma \right) \beta_j. \quad (\text{B.8})$$

As usual, the domain integral is evaluated numerically after splitting it into n_{el} element contributions

$$a(u^h, v^h) = \sum_{k=1}^{n_{el}} \left(\sum_{i=1}^{n_N} \sum_{j=1}^{n_N} \alpha_i \left(\int_{\Omega_k} \nabla N_i \nabla N_j \, d\Omega_k + \gamma \int_{(\Gamma_D)_k} N_i N_j \, d\Gamma_k - \int_{(\Gamma_D)_k} (N_i (\nabla N_j \cdot \mathbf{n}) + N_j (\nabla N_i \cdot \mathbf{n})) \, d\Gamma_k \right) \beta_j \right). \quad (\text{B.9})$$

Appendix C. Mesh refinement

We use for the unstructured quadrilateral mesh the refinement scheme by Toshniwal [58]. Given a set of mixed B-spline control vertices from the coarse Bézier mesh, the objective is to obtain a new set of mixed B-spline control vertices for defining the refined Bézier mesh. Away from the 1-neighbourhood of an extraordinary vertex, that is, where a tensor product structure is locally present, the knot insertion algorithm is used. The refinement of the 1-neighbourhood of an extraordinary vertex of valence v consists of three steps shown in Figure C.25. First, the $v \times 3$ mixed B-spline control vertices at the 2-neighbourhood of the refined Bézier mesh are obtained from the knot insertion algorithm as shown in Figure C.25a. As a result, only the v mixed B-spline control vertices at the 1-neighbourhood of the refined Bézier mesh remain to be selected. In particular, the remaining v mixed B-spline control vertices are selected such that the v midpoints of the edges at the 1-neighbourhood of the coarse Bézier mesh are interpolated. Therefore, the second step is to estimate the midpoints shown in Figure C.25b using, for instance, a root-finding algorithm together with a parametrisation for the edge length. Subsequently, in the third step a $v \times v$ linear system of equations is solved for the v mixed B-spline control vertices at the 1-neighbourhood of the refined Bézier mesh shown in Figure C.25c.

The $v \times v$ linear system is invertible for the case of odd valences $v = 3, 5, \dots$ but not the case of even valences $v = 6, 8, \dots$. For even valences, the $v \times v$ linear system has a rank of $v - 1$. For the case of even valences, following [58] we constraint 1 of the v mixed B-spline control vertices so that the $v \times v$ linear system has a unique solution. Evidently, the choice of the constrained mixed B-spline control vertex is not arbitrary. For instance, choosing to constraint a mixed B-spline control vertex that is far away from the extraordinary vertex can distort the refined Bézier mesh. To avoid any mesh distortion, in this paper, we first select 1 of the v extraordinary elements from the coarse Bézier mesh. After that, assuming that the extraordinary vertex is located at the reference element origin $\boldsymbol{\eta} = (0, 0)$ of the selected extraordinary element, we constraint the mixed B-spline control vertex at $\boldsymbol{\eta} = (\eta_1, \eta_2)$ where η_1 and η_2 are decided case by case, i.e. depending on the coarse Bézier mesh. For example, in Section 5.3, we observe that the choice of $\eta_1 = \eta_2$ with $0.125 \leq \eta_1 \leq 0.25$ generally preserves the mesh quality after refinement.

Appendix D. Arbitrary joint and prism valences

We briefly demonstrate that the approach discussed in Section 4.2.2 applies to an extraordinary joint with arbitrary edge valences e and vertex valence v . As a concrete example, Figure D.26 illustrates the construction of weight functions for an unstructured hexahedral mesh of a truncated box domain with a spherical cavity. The unstructured

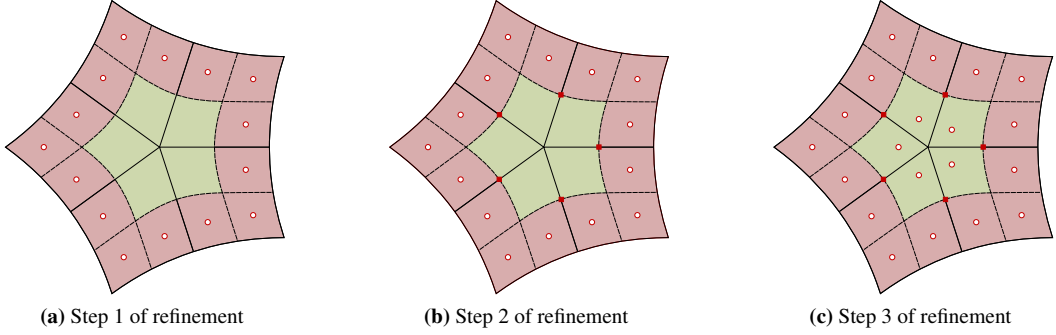


Figure C.25: Refinement of the 1-neighbourhood of an extraordinary vertex with valence $v = 5$. The element boundaries of the coarse and the refined Bézier meshes are depicted as solid line and dashed line, respectively. The refinement scheme consists of three steps. First, the 2-neighbourhood mixed B-spline control vertices of the refined Bézier mesh shown in (a) are obtained using tensor-product knot insertion. Second, we compute the midpoints such that the curve lengths of the 1-neighbourhood edges of the coarse Bézier mesh are approximately bisected shown in (b). Third, the 1-neighbourhood mixed B-spline control vertices of the refined Bézier mesh shown in (c) are computed such that the midpoints determined in (b) are interpolated.

hexahedral mesh shown in D.26a consists of one set of extraordinary edges of valence $e = 3$ and three sets of extraordinary edges of valence $e = 5$ shown in D.26b. The valences of the extraordinary edges can be verified from the extraordinary hexahedra of the mesh shown in D.26c. Overall, the unstructured hexahedral mesh consists of an extraordinary joint where the extraordinary edges of valence $e = 3$ and $e = 5$ meet at a vertex of valence $v = 10$. As discussed in Section 4.2.2, we first require that the support of the prism weight functions do not overlap at the extraordinary joint, see Figure D.26d depicting the union of the prism weight function supports. Subsequently, the extraordinary joint weight function is defined over the set of hexahedra in Figure D.26e. Conceptually, the extraordinary joint weight function defined over the set of hexahedra in Figure D.26e resembles that shown in Figure 14a.

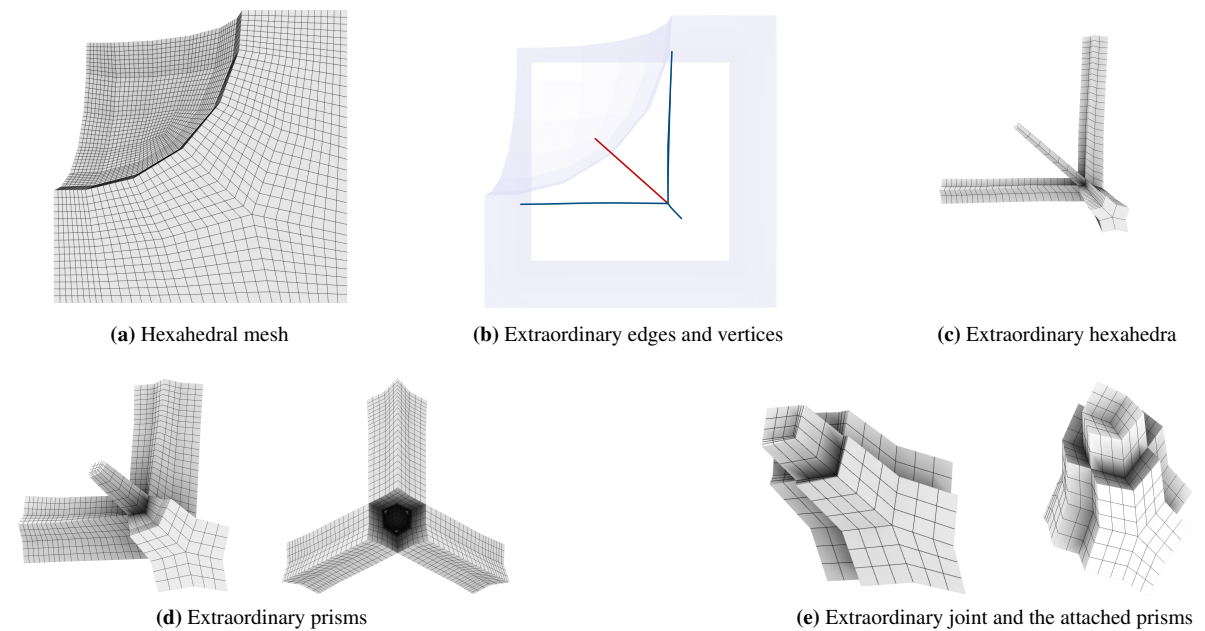


Figure D.26: Truncated box domain with a spherical cavity and (a) its discretisation with an unstructured hexahedral mesh, (b) extraordinary edges and vertices of the mesh, (c) extraordinary hexahedra, (d) extraordinary prisms and (e) extraordinary joint and the attached prisms. In (b) the four sets of extraordinary edges of valence $e = 3$ and $e = 5$ are coloured in red and blue, respectively.

References

- [1] P. Fischer, M. Klassen, J. Mergheim, P. Steinmann, R. Müller, Isogeometric analysis of 2D gradient elasticity, *Computational Mechanics* 47 (3) (2011) 325–334.
- [2] S. Rudraraju, A. Van der Ven, K. Garikipati, Three-dimensional isogeometric solutions to general boundary value problems of Toupin's gradient elasticity theory at finite strains, *Computer Methods in Applied Mechanics and Engineering* 278 (2014) 705–728.
- [3] J. Niiranen, S. Khakalo, V. Balobanov, A. H. Niemi, Variational formulation and isogeometric analysis for fourth-order boundary value problems of gradient-elastic bar and plane strain/stress problems, *Computer Methods in Applied Mechanics and Engineering* 308 (2016) 182–211.
- [4] R. de Borst, C. V. Verhoosel, Gradient damage vs phase-field approaches for fracture: Similarities and differences, *Computer Methods in Applied Mechanics and Engineering* 312 (2016) 78–94.
- [5] D. Codony, O. Marco, S. Fernández-Méndez, I. Arias, An immersed boundary hierarchical B-spline method for flexoelectricity, *Computer Methods in Applied Mechanics and Engineering* 354 (2019) 750–782.
- [6] H. Gómez, V. M. Calo, Y. Bazilevs, T. J. R. Hughes, Isogeometric analysis of the Cahn–Hilliard phase-field model, *Computer Methods in Applied Mechanics and Engineering* 197 (2008) 4333–4352.
- [7] L. Dedè, M. J. Borden, T. J. R. Hughes, Isogeometric analysis for topology optimization with a phase field model, *Archives of Computational Methods in Engineering* 19 (2012) 427–465.
- [8] J. Liu, L. Dede, J. A. Evans, M. J. Borden, T. J. R. Hughes, Isogeometric analysis of the advective Cahn–Hilliard equation: spinodal decomposition under shear flow, *Journal of Computational Physics* 242 (2013) 321–350.
- [9] F. Cirak, M. Ortiz, P. Schröder, Subdivision surfaces: A new paradigm for thin-shell finite-element analysis, *International Journal for Numerical Methods in Engineering* 47 (2000) 2039–2072.
- [10] J. Kiendl, K.-U. Bletzinger, J. Linhard, R. Wüchner, Isogeometric shell analysis with Kirchhoff–Love elements, *Computer Methods in Applied Mechanics and Engineering* 198 (2009) 3902–3914.
- [11] D. J. Benson, Y. Bazilevs, M.-C. Hsu, T. J. R. Hughes, A large deformation, rotation-free, isogeometric shell, *Computer Methods in Applied Mechanics and Engineering* 200 (13–16) (2011) 1367–1378.
- [12] A. Bartezzaghi, L. Dedè, A. Quarteroni, Isogeometric analysis of high order partial differential equations on surfaces, *Computer Methods in Applied Mechanics and Engineering* 295 (2015) 446–469.
- [13] Q. Long, P. B. Bornemann, F. Cirak, Shear-flexible subdivision shells, *International Journal for Numerical Methods in Engineering* 90 (2012) 1549–1577.
- [14] R. Echter, B. Oesterle, M. Bischoff, A hierachic family of isogeometric shell finite elements, *Computer Methods in Applied Mechanics and Engineering* 254 (2013) 170–180.
- [15] P. Murdoch, S. Benzley, T. Blacker, S. A. Mitchell, The spatial twist continuum: A connectivity based method for representing all-hexahedral finite element meshes, *Finite Elements in Analysis and Design* 28 (2) (1997) 137–149.
- [16] M. Tarini, K. Hormann, P. Cignoni, C. Montani, Polycube-maps, *ACM Transactions on Graphics (TOG)* 23 (3) (2004) 853–860.
- [17] M. Nieser, U. Reitebuch, K. Polthier, Cubecover—parameterization of 3D volumes, *Computer Graphics Forum* 30 (2011) 1397–1406.
- [18] J. F. Shepherd, C. R. Johnson, Hexahedral mesh generation constraints, *Engineering with Computers* 24 (3) (2008) 195–213.
- [19] Y. Li, Y. Liu, W. Xu, W. Wang, B. Guo, All-hex meshing using singularity-restricted field, *ACM Transactions on Graphics (TOG)* 31 (2012) 1–11.
- [20] Y. J. Zhang, Geometric modeling and mesh generation from scanned images, Chapman and Hall/CRC, 2018.
- [21] M. Bracci, M. Tarini, N. Pietroni, M. Livesu, P. Cignoni, HexaLab.net: An online viewer for hexahedral meshes, *Computer-Aided Design* 110 (2019) 24–36.
- [22] P. Zhang, J. Vekhter, E. Chien, D. Bommes, E. Vouga, J. Solomon, Octahedral Frames for Feature-Aligned Cross Fields, *ACM Transactions on Graphics (TOG)* 39 (3) (2020) 1–13.
- [23] M. Livesu, N. Pietroni, E. Puppo, A. Sheffer, P. Cignoni, LoopyCuts: practical feature-preserving block decomposition for strongly hex-dominant meshing, *ACM Transactions on Graphics (TOG)* 39 (4) (2020) 121–1.
- [24] T. D. DeRose, Necessary and sufficient conditions for tangent plane continuity of Bézier surfaces, *Computer Aided Geometric Design* 7 (1–4) (1990) 165–179.
- [25] U. Reif, TURBS—topologically unrestricted rational B-splines, *Constructive Approximation* 14 (1998) 57–77.
- [26] M. A. Scott, D. C. Thomas, E. J. Evans, Isogeometric spline forests, *Computer Methods in Applied Mechanics and Engineering* 269 (2014) 222–264.
- [27] T. Nguyen, K. Karčiauskas, J. Peters, C^1 finite elements on non-tensor-product 2D and 3D manifolds, *Applied Mathematics and Computation* 272 (2016) 148–158.
- [28] A. Collin, G. Sangalli, T. Takacs, Analysis-suitable G^1 multi-patch parametrizations for C^1 isogeometric spaces, *Computer Aided Geometric Design* 47 (2016) 93–113.
- [29] D. Toshniwal, H. Speleers, T. J. R. Hughes, Smooth cubic spline spaces on unstructured quadrilateral meshes with particular emphasis on extraordinary points: Geometric design and isogeometric analysis considerations, *Computer Methods in Applied Mechanics and Engineering* 327 (2017) 411–458.
- [30] D. Toshniwal, H. Speleers, R. R. Hiemstra, T. J. R. Hughes, Multi-degree smooth polar splines: A framework for geometric modeling and isogeometric analysis, *Computer Methods in Applied Mechanics and Engineering* 316 (2017) 1005–1061.
- [31] M. Kapl, F. Buchegger, M. Bercovier, B. Jüttler, Isogeometric analysis with geometrically continuous functions on planar multi-patch geometries, *Computer Methods in Applied Mechanics and Engineering* 316 (2017) 209–234.
- [32] M. Kapl, G. Sangalli, T. Takacs, Construction of analysis-suitable G^1 planar multi-patch parameterizations, *Computer-Aided Design* 97 (2018) 41–55.
- [33] K. Karčiauskas, J. Peters, Multi-sided completion of C^2 bi-3 and C^1 bi-2 splines: A unifying approach, *Computer Aided Geometric Design* 86 (2021) 101978.

[34] D. Doo, M. Sabin, Behavior of recursive division surfaces near extraordinary points, *Computer-Aided Design* 10 (1978) 356–360.

[35] E. Catmull, J. Clark, Recursively generated B-spline surfaces on arbitrary topological meshes, *Computer-Aided Design* 10 (1978) 350–355.

[36] J. Peters, U. Reif, *Subdivision Surfaces*, Springer, 2008.

[37] X. Wei, Y. J. Zhang, T. J. R. Hughes, M. A. Scott, Truncated hierarchical Catmull–Clark subdivision with local refinement, *Computer Methods in Applied Mechanics and Engineering* 291 (2015) 1–20.

[38] X. Wei, X. Li, Y. J. Zhang, T. J. R. Hughes, Tuned hybrid nonuniform subdivision surfaces with optimal convergence rates, *International Journal for Numerical Methods in Engineering* 122 (9) (2021) 2117–2144.

[39] Q. Zhang, M. Sabin, F. Cirak, Subdivision surfaces with isogeometric analysis adapted refinement weights, *Computer-Aided Design* 102 (2018) 104–114.

[40] Y. Ma, W. Ma, A subdivision scheme for unstructured quadrilateral meshes with improved convergence rate for isogeometric analysis, *Graphical Models* 106 (2019) 101043.

[41] C. M. Grimm, J. F. Hughes, Modeling surfaces of arbitrary topology using manifolds, in: *SIGGRAPH 1995 Conference Proceedings*, 359–368, 1995.

[42] G. Della Vecchia, B. Jüttler, M.-S. Kim, A construction of rational manifold surfaces of arbitrary topology and smoothness from triangular meshes, *Computer Aided Geometric Design* 25 (2008) 801–815.

[43] L. Ying, D. Zorin, A simple manifold-based construction of surfaces of arbitrary smoothness, *ACM Transactions on Graphics (TOG)* 23 (2004) 271–275.

[44] E. Tosun, D. Zorin, Manifold-based surfaces with boundaries, *Computer Aided Geometric Design* 28 (2011) 1–22.

[45] M. Majeed, F. Cirak, Isogeometric analysis using manifold-based smooth basis functions, *Computer Methods in Applied Mechanics and Engineering* 316 (2017) 547–567.

[46] Q. Zhang, F. Cirak, Manifold-based isogeometric analysis basis functions with prescribed sharp features, *Computer Methods in Applied Mechanics and Engineering* 359 (2020) 112659.

[47] Q. Zhang, T. Takacs, F. Cirak, Manifold-based B-splines on unstructured meshes, in: *Conference on Isogeometric Analysis and Applications*, Springer, 243–262, 2018.

[48] C. Bajaj, S. Schaefer, J. Warren, G. Xu, A subdivision scheme for hexahedral meshes, *The Visual Computer* 18 (2002) 343–356.

[49] Y.-S. Chang, K. T. McDonnell, H. Qin, A new solid subdivision scheme based on box splines, in: *Proceedings of the Seventh ACM Symposium on Solid Modeling and Applications*, 226–233, 2002.

[50] J. Xie, J. Xu, Z. Dong, G. Xu, C. Deng, B. Mourrain, Y. J. Zhang, Interpolatory Catmull–Clark volumetric subdivision over unstructured hexahedral meshes for modeling and simulation applications, *Computer Aided Geometric Design* 80 (2020) 101867:1–101867:16.

[51] U. Reif, M. A. Sabin, Old problems and new challenges in subdivision, *Journal of Computational and Applied Mathematics* 349 (2019) 523–531.

[52] J. Peters, Refinable tri-variate C^1 splines for box-complexes including irregular points and irregular edges, *Computer Aided Geometric Design* 80 (2020) 101877.

[53] X. Wei, Y. J. Zhang, D. Toshniwal, H. Speleers, X. Li, C. Manni, J. A. Evans, T. J. R. Hughes, Blended B-spline construction on unstructured quadrilateral and hexahedral meshes with optimal convergence rates in isogeometric analysis, *Computer Methods in Applied Mechanics and Engineering* 341 (2018) 609–639.

[54] T. Schneider, J. Dumas, X. Gao, M. Botsch, D. Panozzo, D. Zorin, Poly-spline finite-element method, *ACM Transactions on Graphics (TOG)* 38 (3) (2019) 1–16.

[55] T. Schneider, D. Panozzo, X. Zhou, Isogeometric high order mesh generation, *Computer Methods in Applied Mechanics and Engineering* 386 (2021) 114104.

[56] D. Wang, H. Zhang, A consistently coupled isogeometric–meshfree method, *Computer Methods in Applied Mechanics and Engineering* 268 (2014) 843–870.

[57] E. Febranti, M. Ortiz, F. Cirak, Mollified finite element approximants of arbitrary order and smoothness, *Computer Methods in Applied Mechanics and Engineering* 373 (2021) 113513.

[58] D. Toshniwal, Quadratic splines on quad-tri meshes: Construction and an application to simulations on watertight reconstructions of trimmed surfaces, *Computer Methods in Applied Mechanics and Engineering* 388 (2022) 114174.

[59] J. M. Melenk, I. Babuška, The partition of unity finite element method: basic theory and applications, *Computer Methods in Applied Mechanics and Engineering* 139 (1996) 289–314.

[60] J. Nitsche, Über ein Variationsprinzip zur Lösung von Dirichlet-Problemen bei Verwendung von Teilräumen, die keinen Randbedingungen unterworfen sind, *Abhandlungen aus dem Mathematischen Seminar der Universität Hamburg* 36 (1971) 9–15.

[61] S. Fernandez-Mendez, A. Huerta, Imposing essential boundary conditions in mesh-free methods, *Computer Methods in Applied Mechanics and Engineering* 193 (2004) 1257–1275.

[62] A. Emba, J. Dolbow, I. Harari, Imposing Dirichlet boundary conditions with Nitsche’s method and spline-based finite elements, *International Journal for Numerical Methods in Engineering* 83 (7) (2010) 877–898.